

Uniaxial-strain Control of Nematic Superconductivity in $\text{Sr}_x\text{Bi}_2\text{Se}_3$

Ivan Kostylev^{1*}, Shingo Yonezawa^{1*}, Zhiwei Wang^{2,3}, Yoichi Ando², Yoshiteru Maeno¹

¹*Department of Physics, Graduate School of Science, Kyoto University, Kyoto 606-8502, Japan*

²*Institute of Physics II, University of Cologne, Köln 50937, Germany*

³*Key Laboratory of Advanced Optoelectronic Quantum Architecture and Measurement, Ministry of Education (MOE), School of Physics, Beijing Institute of Technology, Beijing 100081, P. R. China*

*e-mail: kostylev@scphys.kyoto-u.ac.jp, yonezawa@scphys.kyoto-u.ac.jp

Nematic states are characterized by rotational symmetry breaking without translational ordering¹⁻⁴. Recently, nematic superconductivity, in which the superconducting gap spontaneously lifts the rotational symmetry of the lattice, has been discovered⁵⁻¹⁰. However the pairing mechanism and the mechanism determining the nematic orientation remain unresolved. A first step is to demonstrate control of the nematicity, through application of an external symmetry-breaking field, to determine the sign and strength of coupling to the lattice. Here, we report for the first time control of the nematic orientation of the superconductivity of $\text{Sr}_x\text{Bi}_2\text{Se}_3$, through externally-applied uniaxial stress. The suppression of subdomains indicates that it is the Δ_{4y} state that is most favoured under compression along the basal Bi-Bi bonds. These results provide an inevitable step towards understanding the microscopic origin of the unique topological nematic superconductivity.

In nematic states of liquid crystals, bar-shaped molecules exhibit orientational ordering and forms thread-like topological defects of the order parameter. Because of the peculiar “partial ordering” property, the orientation of the molecules and hence the structure around defects are easily controlled by external stimuli, as widely utilized in liquid-crystal displays. Analogous phenomena in electronic systems, nematic electron liquids, where conduction electrons exhibit orientational ordering, have been revealed^{1,2}. Here, orientational properties are also highly controllable, and

observations of such tunability have played fundamental roles to clarify driving mechanisms^{3,4}.

A more exotic form of nematicity has been discovered in $A_x\text{Bi}_2\text{Se}_3$ ($A = \text{Cu}, \text{Sr}, \text{Nb}$)⁵⁻⁹: nematic superconductivity⁵, in which the superconducting (SC) gap amplitude spontaneously lifts the rotational symmetry of the lattice. A consensus has been established that the gap has two-fold rotational symmetry, while the lattice has a three-fold rotational symmetry¹⁰. However for definitive demonstration it is essential to show control over the nematic orientation.

In this Letter, we report the first control of nematic superconductivity in $\text{Sr}_x\text{Bi}_2\text{Se}_3$, through application of in situ tunable uniaxial stress along the a axis (meaning a Bi-Bi bond direction). We reversibly controlled the nematic domain structure, allowing us to determine the sign of the coupling constant between the nematicity and lattice distortion.

Our target materials family $A_x\text{Bi}_2\text{Se}_3$ is derived from the topological insulator Bi_2Se_3 ^{11,12}, which has a trigonal crystalline symmetry with three equivalent crystalline a axes in the basal plane (Fig. 1a)¹³. Because the superconductivity induced by A ion intercalation¹⁴⁻¹⁶ occurs in its topologically non-trivial bands^{17,18}, the resultant superconductivity can also be topologically non-trivial. Indeed, topological SC states have been proposed, among which a pair of SC states in the two-dimensional E_u representation, Δ_{4x} and Δ_{4y} , are nematic SC states^{5,19-21}. The SC gap amplitude of the Δ_{4x} and Δ_{4y} states are two-fold anisotropic and their maximum amplitude is located along the a and a^* axes, respectively (Fig. 1a). It has been shown that there is sample-to-sample variation in whether the nematicity aligns along a a or a^* axis²². This fact suggests that Δ_{4x} and Δ_{4y} states are nearly degenerate states, such that the preferred state can be selected by a certain pre-existing symmetry breaking field such as possible structural distortion or A ion distribution. Here, we probe whether applied uniaxial stress can overcome this pinning.

Another important issue is the pairing mechanism in $A_x\text{Bi}_2\text{Se}_3$. This material is quite exceptional in the sense that it exhibits unconventional superconductivity without any proximity to magnetic or electric orderings and without strong electron-electron correlations²³. Uniaxial strain

effects provides hints toward examination of various pairing scenarios.

In this work, we measured the magnetoresistance of single-crystalline $\text{Sr}_{0.06}\text{Bi}_2\text{Se}_3$ samples (with the critical temperature T_c of 2.8 K; see Supplementary Note S1) under uniaxial strain. The sample was affixed onto a custom-made uniaxial strain cell²⁴, a modified version of the recent invention²⁵, mounted inside a vector magnet. The sample was cut along one of the a axes (Bi-Bi bond direction), which we define as the x axis (Figs. 1a and b). Both the uniaxial force and electric current were applied along this x axis. The angle between the magnetic field and x axis is denoted as ϕ_{ab} .

In Figs. 1c, 2a, and 2b, we present the magnetoresistance at 2.2 K for various ϕ_{ab} . First, focus on the data with the relative strain $\Delta\epsilon_{xx}$ of 0%, i.e. zero applied voltage to the piezo stacks (black curves in Fig. 1c), corresponding to the actual strain of around +0.10% (tensile) due to the thermal-contraction difference of the sample and strain cell (Methods). Clearly, superconductivity is more stable for $\phi_{ab} = -90^\circ$ ($H \parallel -y$) than 0° ($H \parallel x$), resulting in a prominent two-fold upper critical field H_{c2} , which is indicative of the nematic superconductivity^{8,22}. This observed anisotropy $H_{c2} \parallel -y > H_{c2} \parallel x$ is consistent with the Δ_{4y} state with the SC gap larger along y ²⁶, which is schematically shown as the Y_0 state in Fig. 2c. Interestingly, additional six-fold behavior emerges at the onset of the SC transition between 1 and 2 T, as clearly visible by the green region extending along $\phi_{ab} = -30^\circ$ or $+30^\circ$ in Fig. 2a (See Supplementary Fig. S2 for raw data). This six-fold component indicates that the sample contains minor parts exhibiting large H_{c2} along $\phi_{ab} = \pm 30^\circ$, namely the Y_1 and Y_2 domains (Δ_{4y}) in Fig. 2c with their gap maxima along the $\pm 30^\circ$ directions.

Next, let us focus on the data under applied strain of $\Delta\epsilon_{xx} = -1.19\%$ (green curves in Fig. 1c) corresponding to the actual compressive strain of around $\epsilon_{xx} \simeq -1.1\%$; the largest measured compressive strain in the elastic limit (see Supplementary Note S3). Notably, the magnetoresistance at the SC transition is substantially altered, marking the first in-situ uniaxial-strain control of nematic superconductivity. More specifically, the SC transition becomes sharper with strain except near $\phi_{ab} = -90^\circ$ ($H \parallel y$). Moreover, comparing the color plots in Figs. 2a and b, we can notice that the

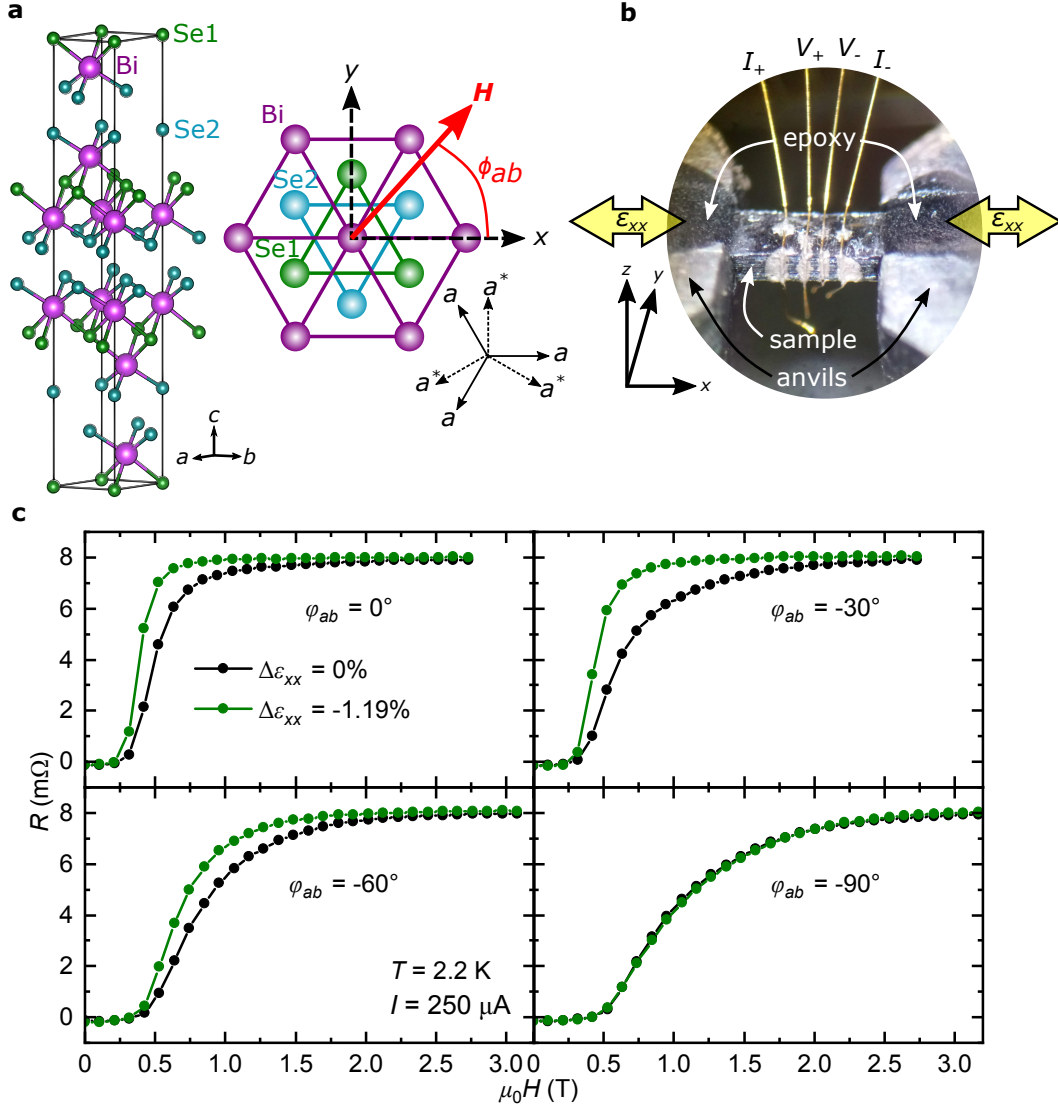


Figure 1: Uniaxial-strain control of nematic superconductivity in $\text{Sr}_x\text{Bi}_2\text{Se}_3$. **a**, Crystal structure of the mother compound Bi_2Se_3 . The right figure shows the definitions of the axes and the field angle ϕ_{ab} with respect to the crystal structure in the ab plane, with three equivalent a - and a^* -axes. **b**, Photograph of the sample in the uniaxial strain cell with 4-wire terminal configuration. I and V labels next to the gold wires indicate the current and voltage leads, respectively. The large yellow arrows indicate the direction of the external strain, which was applied parallel to the x axis. **c**, Magnetoresistance at specified field directions in the ab plane ($\phi_{ab}=0^\circ, -30^\circ, -60^\circ, -90^\circ$), with and without $\Delta\epsilon_{xx}$. The data were obtained at 2.2 K and with 250 μA applied current. A substantial change in the magnetoresistance curves under large $\Delta\epsilon_{xx}$ (green curves) provides evidence for the in-situ uniaxial-strain control of the nematic superconductivity.

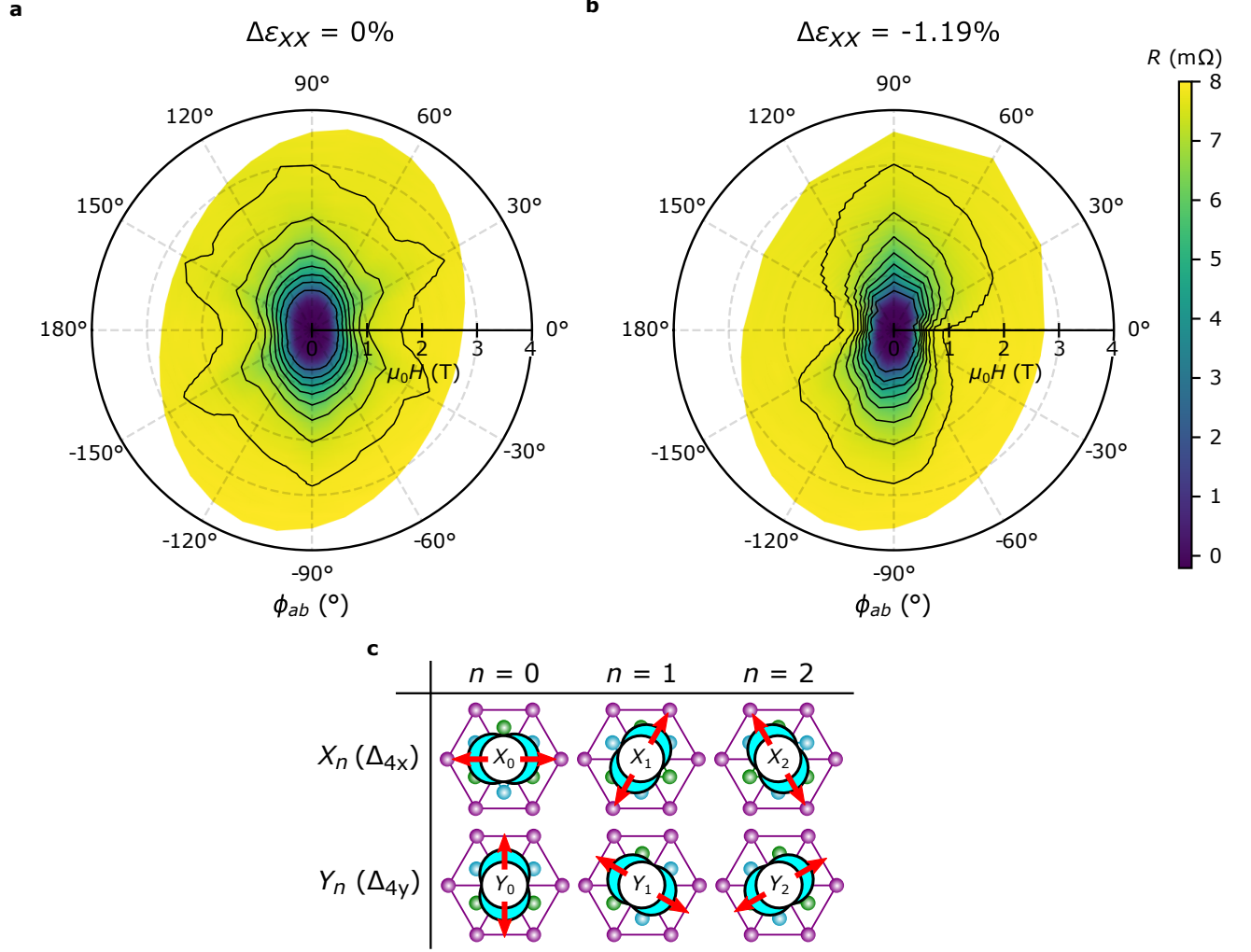


Figure 2: Disappearance of nematic superconducting domains in $\text{Sr}_x\text{Bi}_2\text{Se}_3$ under compressive strain.

a and **b**, Color polar plot of magnetoresistance for $H \parallel ab$ measured at the relative strains of $\Delta\epsilon_{xx} = 0$ (**a**) and -1.19% (**b**) with $250 \mu\text{A}$ applied current and 2.2 K . The light-green regions extending along $\pm 30^\circ$ and $\pm 150^\circ$ in **a** indicate existence of nematic subdomains, which substantially disappears under applied strain (**b**). The contours are drawn from $0.5 \text{ m}\Omega$ to $7.5 \text{ m}\Omega$ in steps of $1 \text{ m}\Omega$. **c**, Table of the 6 possible nematic superconducting states that can exist in the sample as domains. X_n and Y_n ($n = 0, 1, 2$) domains exhibit Δ_{4x} and Δ_{4y} states with the large H_{c2} along one of the a axes ($\phi_{ab} = (60n)^\circ$) and a^* axes ($\phi_{ab} = (90 + 60n)^\circ$), respectively, as indicated with the red arrows. The crystal structure in the ab plane of Bi_2Se_3 is shown with the schematic superconducting wave function in its center. The thickness of the blue crescent depicts the superconducting gap amplitude.

weak six-fold SC onset due to domains, seen in the $\Delta\epsilon_{xx} = 0$ data, is substantially reduced by the applied strain. Thus the primary effect of the compressive uniaxial strain is to suppress the minor nematic domains.

From the magnetoresistance data, we defined H_{c2} as the field where the resistance $R(H)$ divided by the normal-state resistance R_n reaches various criterion values (Methods; Supplementary Note S4). In the strain dependence of H_{c2} (Fig. 3), there is a high reproducibility among measurement cycles within the present strain range, manifesting that strain response is repeatable and thus our sample is in the elastic deformation regime. Reproducibility across samples has also been demonstrated (see Supplementary Note S5).

Comparing data for various field directions, we can see that $H_{c2} \parallel x$ largely reduces under strain, attributable to the disappearance of minor nematic SC domains. In contrast, H_{c2} along the y and z axes (Fig. 3), as well as the zero-field T_c (Supplementary Fig. S7), is only weakly affected by strain, with small decreasing trend under compression.

The strain control of the nematic subdomains is more evident in the $H_{c2}(\phi_{ab})$ curves in Fig. 4a. Notice that H_{c2} defined with higher values of R/R_n is more sensitive to existence of nematic sub domains. In addition to the prominent two-fold anisotropy with maxima at $\phi_{ab} = \pm 90^\circ$ (Y_0 domain) seen in all criteria, H_{c2} with the 95% or 80% criteria exhibit additional 4 peaks located at $\phi_{ab} = \pm 30^\circ$ and $\pm 150^\circ$ for low $\Delta\epsilon_{xx}$, due to the existence of Y_1 and Y_2 domains. These peaks are suppressed with increasing $\Delta\epsilon_{xx}$, indicating the disappearance of the minor Y_1/Y_2 domains. In contrast, in H_{c2} with lower criteria, the additional peaks are absent because the sample resistivity near the zero resistance state is mostly governed by the domain with the highest volume fraction. Nevertheless, even for H_{c2} with the lower criteria (e.g. $R/R_n = 5\%$), there is noticeable strain dependence near $\phi_{ab} = 0^\circ$. This dependence is also attributable to the domain change by comparison with a model simulation explained next.

In this simulation, we assume a network consisting of many Y_0 domains and one of each

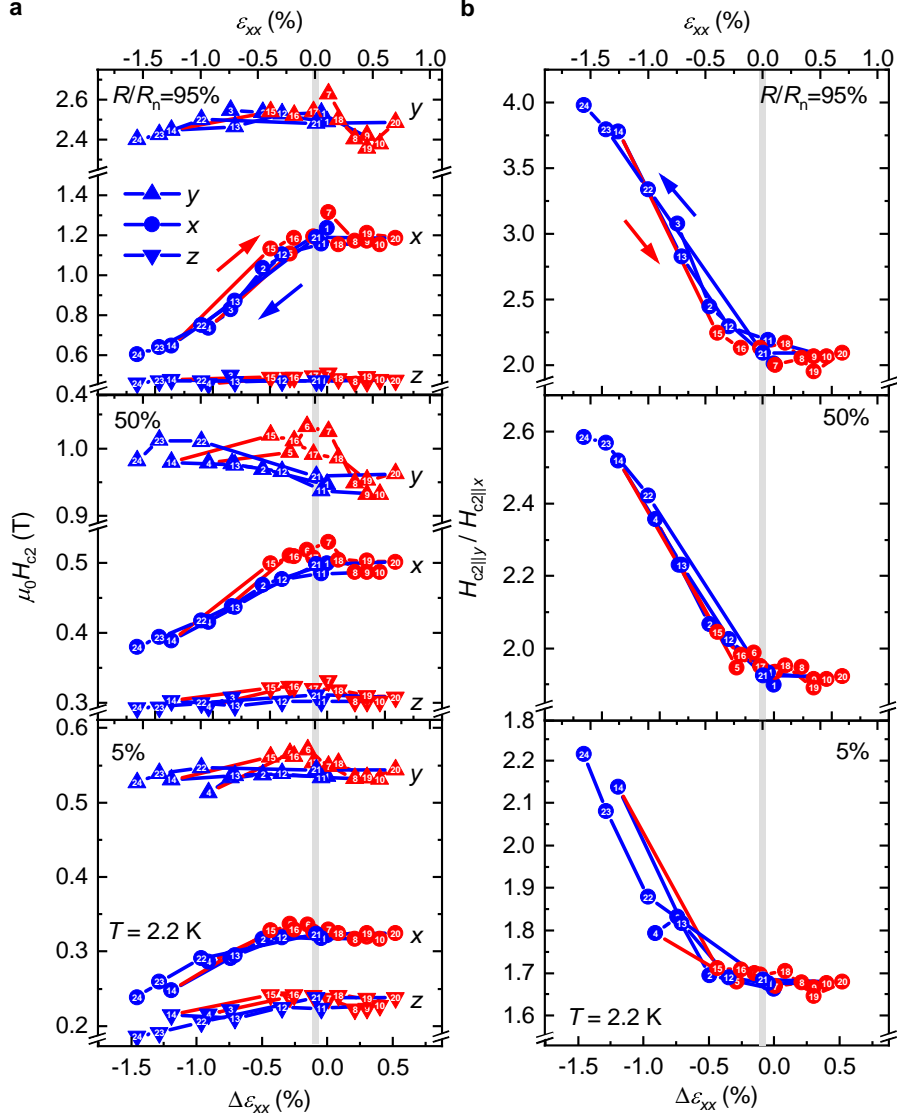


Figure 3: Reversible uniaxial-strain control of the nematic superconductivity. **a**, Upper critical field (H_{c2}) at 2.2 K along the a axis (x ; $\phi_{ab}=0^\circ$; \bullet), a^* axis (y ; $\phi_{ab}=-90^\circ$; \blacktriangle), c axis (z ; \blacktriangledown), as a function of the relative strain $\Delta\epsilon_{xx}$ induced by an applied voltage to the piezostacks. **b**, In-plane H_{c2} anisotropy $H_{c2||y}/H_{c2||x}$ as a function of strain. At the top of each panel, the estimated actual strain $\epsilon_{xx} \simeq \Delta\epsilon_{xx} + 0.1\%$ is indicated (see Methods) and the gray region illustrates the possible range in the actual zero strain. The numbers in the top corner of each sub-panel indicates the criteria used for determining H_{c2} (see Methods) The numbers in the data points indicate the order of the measurements. The blue and red data points indicate the cases that the measurement was performed after a decrease and increase in strain, respectively. Here, the H_{c2} anisotropy varies systematically with external strain.

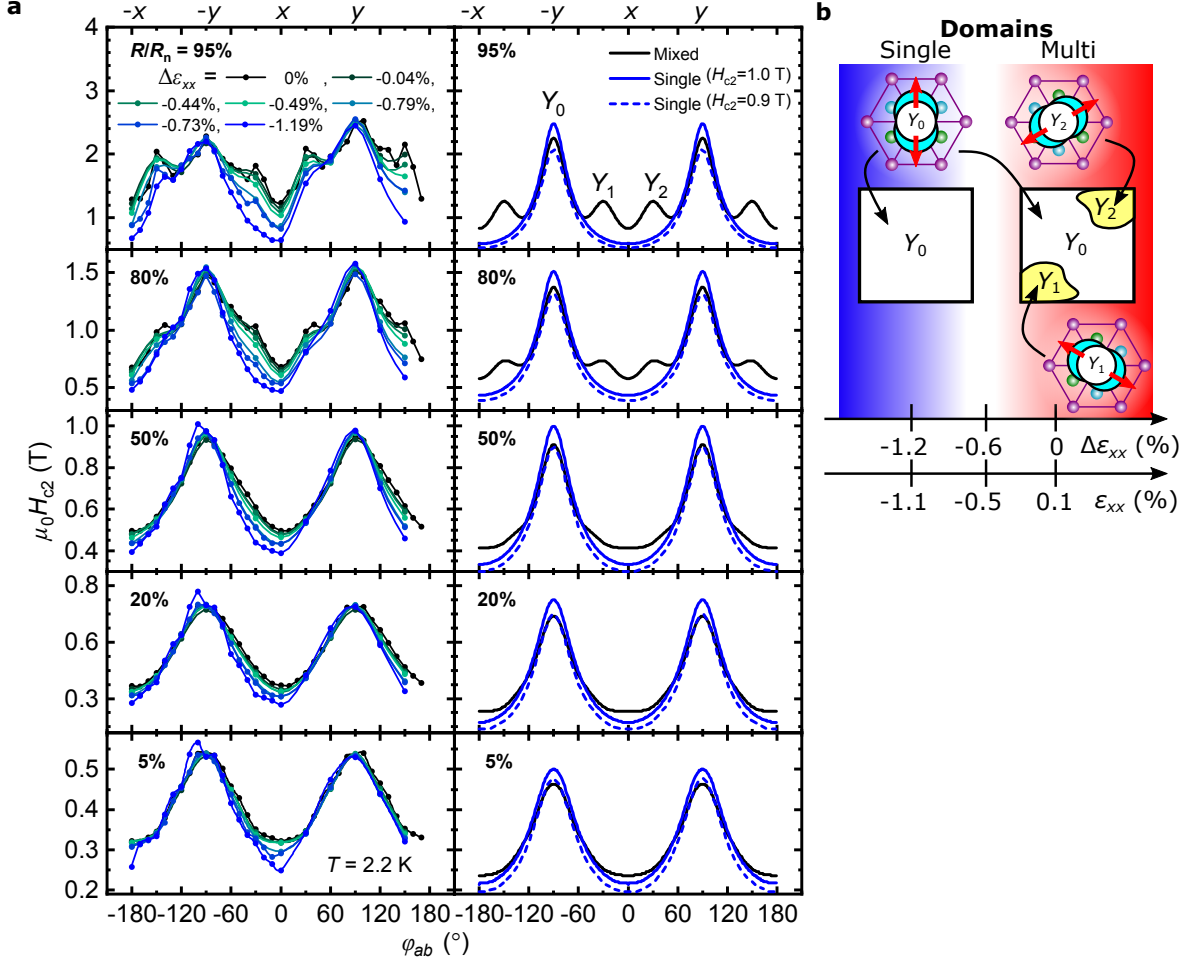


Figure 4: Evidence for the control of nematic superconducting domains with strain. **a**, In-plane field angle ϕ_{ab} dependence of the upper critical field H_{c2} at 2.2 K for various criteria (see Methods), which are indicated with a number in the top-left corner of each sub-panel. The curves colored from black to blue are in the order of increasing compressive strain; the numbers in the legend indicate the value of $\Delta\epsilon_{xx}$. The results of a simulation are shown in the second column (see Methods) capturing key features of the observation. **b**, Schematic showing spatial configurations of nematic superconducting domains controlled in-situ by the uniaxial strain in our experiment. The yellow regions are the minor domains (Y_1 and Y_2), which are suppressed by the application of compressive strain, as evidenced by the changes in the $H_{c2}(\phi_{ab})$ curves.

Y_1/Y_2 domain and calculate the net resistance under magnetic fields (Methods). Then H_{c2} with various criteria is evaluated from the calculated resistivity curves. Under strain, the minor domains are assumed to change into Y_0 domains. As shown in Fig. 4, the simulation reproduces all the observed features described above, even without any change of H_{c2} and in-plane H_{c2} anisotropy in each domain. This leads one to infer that the observed behavior is almost solely explained by the change of the nematic SC subdomains. We find that setting slightly smaller H_{c2} (ca. decrease of 10%; the broken curves in Fig. 4a) of the Y_0 domain under strain gives a better match with the experimental data.

Summarizing our findings, we succeeded in repeatable in-situ uniaxial-strain control of nematic SC domains, covering pre-existing tensile regime to the compressive regime. The primary effect of the increasing compressive strain is the suppression of minor Y_1/Y_2 domains, well reproduced by a simple model simulation. Other properties are rather insensitive to the strain, but there are decreasing trends in T_c as well as H_{c2} of the main domain under compression.

The coupling between the nematic superconductivity and uniaxial strain has been proposed using the Ginzburg-Landau (GL) formalism^{27,28}. The strain couples to the nematic superconductivity through the free energy $F_\varepsilon = g \left[(\varepsilon_{xx} - \varepsilon_{yy})(|\eta_x|^2 - |\eta_y|^2) + 2\varepsilon_{xy}(\eta_x\eta_y^* + \eta_y\eta_x^*) \right]$, where g is the coupling constant, η_x and η_y are the amplitudes of the Δ_{4x} and Δ_{4y} components. This relation indicates that uniaxial ε_{xx} strain prefers one of the Δ_{4x} or Δ_{4y} states, depending on the sign of g . If a pre-existing symmetry breaking field exists, the nematic SC order parameter is initially fixed to the pre-existing field direction but eventually the state most favored by the external strain direction will be chosen with increasing strain. This is true even when the pre-existing field and external strain have a finite angle, as in the case for the Y_1 or Y_2 domains: the nematicity gradually rotates toward the external strain (see Supplementary Fig. S8). However, in these phenomenological theories, the sign of g remains arbitrary and should be determined based on experiments. Our result, a multi-domain sample driven to a mono-domain Δ_{4y} state by $\varepsilon_{xx} < 0$ as shown in Fig. 3c, indicates that g is negative, an important step toward modeling of the nematic SC phenomenon. Moreover, this negative g provides a crucial constraint to realistic microscopic theories on the pairing mechanism.

Such model should explain the observed weak sensitivity of T_c on ε_{xx} . For example, a proposed odd-parity fluctuation model making use of phonons dispersing along the k_z direction^{29–32} can be compatible with our observation, since such k_z phonons should be less sensitive to the in-plane distortions.

Coming back to the GL theories, they predict that T_c linearly increases with increasing strain in either tensile or compressive directions, accompanied by a kink in $T_c(\varepsilon_{xx})$ at the strain where the nematic state changes between Δ_{4x} and Δ_{4y} ^{27,28}. This prediction, at first glance, seems to be inconsistent with our decreasing trend of T_c with increasing $|\varepsilon_{xx}|$. However, we should note that T_c of doped Bi_2Se_3 decreases under hydrostatic pressure, i.e. under isotropic strain³³. This effect is not taken into account in the above mentioned GL free energy, which couples only to the anisotropic strains. In the actual experiments, a combination of the increasing and decreasing trends in T_c due to anisotropic and isotropic strains, respectively, is observed. If the latter is relatively stronger, the observed small decrease of T_c by compressive strain is explained. Moreover, the existence of multiple domains weakens the predicted kink in $T_c(\varepsilon_{xx})$, because each domain's $T_c(\varepsilon_{xx})$ curve convolves. This will result in a rounded kink, further obfuscating the linear behavior predicted from a mono-domain model.

To conclude, we provide the first experimental demonstration of uniaxial-strain control of nematic superconductivity in doped Bi_2Se_3 . Firstly, suppressing minor domains while stabilizing the Δ_{4y} state. Secondly, we determined the sign of the nematic coupling constant. These findings should provide bases toward resolving the open issues of this highly attractive superconductor. Additionally, this work points to possible engineering of topological nematic superconductivity by uniaxial strain.

Methods

Sample preparation and characterization. Single crystals of $\text{Sr}_x\text{Bi}_2\text{Se}_3$ (nominal $x = 0.06$) were grown from high-purity elemental of Sr chunk (99.99%), Bi shot (99.9999%), and Se shots

(99.9999%) by a conventional melt-growth method. The raw materials were mixed with a total weight of 5.0 g and sealed in an evacuated quartz tube. The tube was heated to 1223 K and kept for 48 hours with intermittent shaking to ensure the homogeneity of the melt. Then it was cooled slowly to 873 K at a rate of 4 K/h and finally quenched into ice water. It is worth pointing out that quench is essential for obtaining superconducting samples with high shielding fraction. The sample used here was cut from a large shiny crystal by wire saw, and the size is 4 mm (length) \times 0.53 mm (width) \times 0.5 mm (thickness; along the c axis) with the longest dimension along the a axis.

Strain cell and sample mounting. We constructed a custom-made piezoelectric-based uniaxial strain cell (Ref. 24), based on the design of Ref. 25. The bar-shaped sample was mounted between two anvils by a strong epoxy (Stycast 2850FTJ, Henkel Ablestik Japan Ltd.). The anvils can apply compressive or tensile strain on the sample by applying a positive voltage on the inner or outer piezo stacks, respectively. Thus the strain was applied parallel to the a axis, as shown in Fig. 1. The maximum applied voltage range for each piezo stack was -400 V to 600 V corresponding roughly to -13 μ m to 20 μ m length changes of the piezo stacks used (P-885.11, PI) at cryogenic temperatures. A parallel-plate capacitor was mounted on the anvils to track the distance between the two plates by measuring the capacitance using a capacitance bridge (2500A, Andeen-Hagerling). The strain was then determined by the displacement divided by the exposed sample length, which was 1.14 ± 0.05 mm in this study.

Estimation of the thermally-induced strain. The effect of thermal contraction of the sample and the strain cell should be taken into consideration. Because the materials used in the strain cell are placed symmetrically between the compressive and tensile arms, the thermal strain on the sample originates only from the asymmetric part²⁴; on the compressive arm, the sample with the length L_{sample} of 1.14 mm is placed, but on the tensile arms there are Ti blocks. This 1.14-mm length Ti part shrinks less than the sample, resulting in a tensile strain to the sample after cooling down from the epoxy curing temperature (around 350 K). The shrinkage of the sample $\Delta L_{\text{sample}}/L_{\text{sample}}$ is evaluated as $[a(4 \text{ K}) - a(350 \text{ K})]/a(350 \text{ K}) = -0.36\%$. Here, we used the lattice

constants of Bi_2Se_3 reported in Ref. 34. We note that $a(4\text{ K})$ and $a(350\text{ K})$ is estimated by a linear extrapolation because Ref. 34 reports a values only between 10 K and 270 K. For Ti, the shrinkage $\Delta L_{\text{Ti}}/L_{\text{Ti}}$ is evaluated to be -0.23% by integrating the linear thermal expansion coefficient between 4 K and 350 K reported in Ref. 35. The thermal expansion coefficient at 4 K and 350 K were obtained after linearly extrapolated. Thus, the thermally-induced strain to the sample is tensile and $(\Delta L_{\text{Ti}} - \Delta L_{\text{sample}})/L_{\text{sample}} = +0.13\%$ considering $L_{\text{Ti}} = L_{\text{Sample}}$. In addition, because of the stiffness of the component materials, in particular the epoxy, the actual strain transmitted to the sample may be reduced by roughly 56% ²⁴. Thus, the value $+0.13\%$ should be considered as the upper bound, and the lower bound should be $0.13\% \times 0.56 = 0.07\%$. To conclude, by taking the average, the thermally-induced strain is evaluated to be $0.10 \pm 0.03\%$: the actual strain ε_{xx} is given as $\varepsilon_{xx} \simeq \Delta\varepsilon_{xx} + 0.1\%$, where $\Delta\varepsilon_{xx}$ is the strain applied relative to the situation of zero applied voltage to the piezo stacks.

Resistivity measurement. Sample resistivity was measured by four-terminal sensing: we applied a DC current using a current source (6221, Keithley Instruments) to the two outer wires and measure the resultant voltage by a nanovoltmeter (2182A, Keithley Instruments) on the inner two wires. To subtract the voltage offset, we use the “Delta Mode” of the combined operation of these instruments: the polarity of the current was periodically changed to acquire only the voltage component that is dependent on the current. Au wire (20 μm diameter) were directly connected to the *ac* surface of the sample by Ag paint (4929N, Du Pont). To improve the mechanical stability of the wires, the Au wires were anchored onto the *ab* surface by Ag epoxy (H20E, EPOTEK), which has been confirmed to be electrically insulating to the sample. The four contacts were equispaced by about 0.2 mm. The contact resistance was on the order of 100 Ω at room temperature.

Temperature and magnetic-field control. We used a $^3\text{He}/^4\text{He}$ dilution refrigerator (Kelvinox 25, Oxford Instruments) to cool down the sample. It was inserted into the vector magnet described below. The lowest temperature achievable is roughly 80 mK, well below the superconducting transition temperature of $\sim 2.8\text{ K}$. The temperature was measured using a resistive thermometer (Cernox, Lakeshore) and a resistance bridge (AVS-47, Picowatt). A 350- Ω strain gauge (KFG-1-

350-C1-16, KYOWA), that was used as a heater for temperature control, was mounted close to the strain cell.

We applied the magnetic field using a vector-magnet system³⁶, which consists of two orthogonal superconducting magnets (pointing in the vertical and horizontal directions in the laboratory frame) inside a dewar that rests on a horizontal rotation stage. This system allows us to direct the magnetic field accurately in any direction in space while the refrigerator, as well as the sample, is fixed. The superconducting magnets can apply fields up to 3 T (vertical) and 5 T (horizontal). The magnetic field can be controlled with a resolution of 0.1 mT. The precision of the horizontal rotation of the helium dewar is 0.001° , with negligible backlash. The strain cell was fixed with a sample mounted, so that the a axis is roughly along the vertical direction in the laboratory frame. The precise directions of the crystalline axes with respect to the laboratory frame are determined by making use of the anisotropy in H_{c2} . Once the directions of the crystalline axes are determined, we can rotate the magnetic field within the sample frame. All field angle values presented in this Letter are defined in the sample frame. Refer to Supplementary Note S8 and Fig. S9 for the detailed mathematical explanation for the vector transformations and a demonstration of the field alignment. In addition, see Supplementary Note S9 for the rationale behind the choice of temperature and magnetic field value for the alignment.

Evaluation of H_{c2} . The upper critical field H_{c2} was evaluated by the value of the magnetic field at which the sample resistivity reaches a certain percentage of the normal-state resistivity. If the resistivity value falls in between two data points, then H_{c2} is determined by using linear interpolation. For a more detailed methodology see Supplementary Note S4. Temperature dependence of H_{c2} and its anisotropy is given in Supplementary Note S11.

Model simulation. The experimental $H_{c2}(\phi_{ab})$ curve shows three peaks indicating three nematic domains. Thus, we simulated the H_{c2} behavior of multi and single domain samples by considering an electrical circuit consisting of a network of resistive elements representing the three possible nematic SC domains. For the simulation shown in the main text, the circuit is assumed to be a 3D network (see Supplementary Fig. S13) of 12 elements to model the situation that current passes

from end to end through a 3D distribution of domains. For the multi-domain simulation corresponding to the non-strained sample, the 12 elements are divided into 10 Y_0 nematic domains, and one of each Y_1 and Y_2 domains. The exact positions are described in Supplementary Note S10. For the single-domain simulation corresponding to the highly compressed sample, all the 12 elements are assumed to be Y_0 domains. The calculation of H_{c2} is done as follows: firstly, for a fixed H and ϕ_{ab} , resistivity of each circuit element is calculated from an empirical relationship among resistance, applied magnetic field H and field direction ϕ_{ab} , by taking into account H_{c2} anisotropy of each domain (see Supplementary Note S10 for details). Secondly, the total circuit resistance of the network R_{total} is calculated. The first and second step is iterated while varying H and ϕ_{ab} , to obtain the H dependence of R_{total} for each ϕ_{ab} . Lastly, H_{c2} at ϕ_{ab} is determined from the $R_{\text{total}}(H)$ curve at ϕ_{ab} using the same method as that used for the experimental data analysis (see Supplementary Note S4).

Reference

1. Kivelson, S. A., Fradkin, E. & Emery, V. J. Electronic liquid-crystal phases of a doped Mott insulator. *Nature* **393**, 550 (1998).
2. Fradkin, E., Kivelson, S. A., Lawler, M. J., Eisenstein, J. P. & Mackenzie, A. P. Nematic Fermi Fluids in Condensed Matter Physics. *Ann. Rev. Condens. Matter Phys.* **1**, 153–178 (2010).
3. Chu, J.-H., Kuo, H.-H., Analytis, J. G. & Fisher, I. R. Divergent Nematic Susceptibility in an Iron Arsenide Superconductor. *Science* **337**, 710–712 (2012).
4. Fernandes, R. M., Chubukov, A. V. & Schmalian, J. What drives nematic order in iron-based superconductors? *Nat. Phys.* **10**, 97 (2014).
5. Fu, L. Odd-parity topological superconductor with nematic order: Application to $\text{Cu}_x\text{Bi}_2\text{Se}_3$. *Phys. Rev. B* **90**, 100509(R) (2014).
6. Matano, K., Kriener, M., Segawa, K., Ando, Y. & Zheng, G. Spin-rotation symmetry breaking in the superconducting state of $\text{Cu}_x\text{Bi}_2\text{Se}_3$. *Nat. Phys.* **12**, 852–854 (2016).

7. Yonezawa, S. *et al.* Thermodynamic evidence for nematic superconductivity in $\text{Cu}_x\text{Bi}_2\text{Se}_3$. *Nat. Phys.* **13**, 123–126 (2017).
8. Pan, Y. *et al.* Rotational symmetry breaking in the topological superconductor $\text{Sr}_x\text{Bi}_2\text{Se}_3$ probed by upper-critical field experiments. *Sci. Rep.* **6**, 28632(1–7) (2016).
9. Asaba, T. *et al.* Rotational Symmetry Breaking in a Trigonal Superconductor Nb-doped Bi_2Se_3 . *Phys. Rev. X* **7**, 011009 (2017).
10. Yonezawa, S. Nematic Superconductivity in Doped Bi_2Se_3 Topological Superconductors. *Condens. Matter* **4**, 2 (2019).
11. Xia, Y. *et al.* Observation of a large-gap topological-insulator class with a single Dirac cone on the surface. *Nat. Phys.* **5**, 398–402 (2009).
12. Hsieh, D. *et al.* A tunable topological insulator in the spin helical Dirac transport regime. *Nature* **460**, 1101–1105 (2009).
13. Lind, H. & Lidin, S. A general structure model for BiSe phases using a superspace formalism. *Solid State Sci.* **5**, 47 – 57 (2003).
14. Hor, Y. S. *et al.* Superconductivity in $\text{Cu}_x\text{Bi}_2\text{Se}_3$ and its Implications for Pairing in the Undoped Topological Insulator. *Phys. Rev. Lett.* **104**, 057001 (2010).
15. Shruti, Maurya, V. K., Neha, P., Srivastava, P. & Patnaik, S. Superconductivity by Sr intercalation in the layered topological insulator Bi_2Se_3 . *Phys. Rev. B* **92**, 020506(R) (2015).
16. Qiu, Y. *et al.* Time reversal symmetry breaking superconductivity in topological materials. *arXiv:1512.03519* (2015).
17. Wray, L. A. *et al.* Observation of topological order in a superconducting doped topological insulator. *Nature Phys.* **8**, 855–859 (2010).
18. Lahoud, E. *et al.* Evolution of the Fermi surface of a doped topological insulator with carrier concentration. *Phys. Rev. B* **88**, 195107 (2013).

19. Fu, L. & Berg, E. Odd-Parity Topological Superconductors: Theory and Application to $\text{Cu}_x\text{Bi}_2\text{Se}_3$. *Phys. Rev. Lett.* **105**, 097001 (2010).
20. Sasaki, S. *et al.* Topological Superconductivity in $\text{Cu}_x\text{Bi}_2\text{Se}_3$. *Phys. Rev. Lett.* **107**, 217001 (2011).
21. Sato, M. & Ando, Y. Topological superconductors: a review. *Rep. Prog. Phys.* **80**, 076501 (2017).
22. Du, G. *et al.* Superconductivity with two-fold symmetry in topological superconductor $\text{Sr}_x\text{Bi}_2\text{Se}_3$. *Sci. China Phys. Mech. Astron.* **60**, 037411(1–6) (2017).
23. Kriener, M., Segawa, K., Ren, Z., Sasaki, S. & Ando, Y. Bulk Superconducting Phase with a Full Energy Gap in the Doped Topological Insulator $\text{Cu}_x\text{Bi}_2\text{Se}_3$. *Phys. Rev. Lett.* **106**, 127004 (2011).
24. Kostylev, I., Yonezawa, S. & Maeno, Y. Piezoelectric-based uniaxial strain cell with high strain throughput and homogeneity. *J. Appl. Phys.* **125**, 082535 (2019).
25. Hicks, C. W., Barber, M. E., Edkins, S. D., Brodsky, D. O. & Mackenzie, A. P. Piezoelectric-based apparatus for strain tuning. *Rev. Sci. Instrum.* **85**, 065003 (2014).
26. Tsutsumi, Y., Nomoto, T., Ikeda, H. & Machida, K. Nodal gap detection through polar angle-resolved density of states measurements in uniaxial superconductors. *Phys. Rev. B* **94**, 224503 (2016).
27. Venderbos, J. W. F., Kozii, V. & Fu, L. Identification of nematic superconductivity from the upper critical field. *Phys. Rev. B* **94**, 094522(1–7) (2016).
28. How, P. T. & Yip, S.-K. Signatures of Nematic Superconductivity in Doped Bi_2Se_3 under Applied Stress. *arXiv:1901.11237* (2019).
29. Wan, X. & Savrasov, S. Y. Turning a band insulator into an exotic superconductor. *Nat. Commun.* **5**, 4144 (2014).

30. Brydon, P. M. R., Das Sarma, S., Hui, H.-Y. & Sau, J. D. Odd-parity superconductivity from phonon-mediated pairing: Application to $\text{Cu}_x\text{Bi}_2\text{Se}_3$. *Phys. Rev. B* **90**, 184512 (2014).
31. Wu, F. & Martin, I. Nematic and chiral superconductivity induced by odd-parity fluctuations. *Phys. Rev. B* **96**, 144504 (2017).
32. Wang, J. *et al.* Evidence for singular-phonon-induced nematic superconductivity in a topological superconductor candidate $\text{Sr}_{0.1}\text{Bi}_2\text{Se}_3$. *Nat. Commun.* **10** (2019).
33. Nikitin, A. M., Pan, Y., Huang, Y. K., Naka, T. & de Visser, A. High-pressure study of the basal-plane anisotropy of the upper critical field of the topological superconductor $\text{Sr}_x\text{Bi}_2\text{Se}_3$. *Phys. Rev. B* **94**, 144516(1–5) (2016).
34. Chen, X. *et al.* Thermal expansion coefficients of Bi_2Se_3 and Sb_2Te_3 crystals from 10 K to 270 K. *Appl. Phys. Lett.* **99**, 261912 (2011).
35. Cowan, J., Pawlowicz, A. & White, G. Thermal expansion of polycrystalline titanium and zirconium. *Cryogenics* **8**, 155 – 157 (1968).
36. Deguchi, K., Ishiguro, T. & Maeno, Y. Field-orientation dependent heat capacity measurements at low temperatures with a vector magnet system. *Rev. Sci. Instrum.* **75**, 1188–1193 (2004).

Acknowledgments

The authors acknowledge H.-H. Wen, J. Schmalian, P. T. How, S.-K. Yip, V. Kozii, and J. W. F. Venderbos, H.-S. Xu, and G. Mattoni for valuable discussions. We also acknowledge C. W. Hicks, M. E. Barber, A. Steppke, F. Jerzembeck, and A. P. Mackenzie for sharing their knowledge into the construction of a strain cell. This work was supported by JSPS Grant-in-Aids for Scientific Research on Innovative Areas on “Topological Materials Science” (KAKENHI JP15H05851, JP15H05852, JP15H05853, JP15K21717), by JSPS Grant-in-Aid KAKENHI 17H04848, and by the JSPS Core-to-Core program. The work at Cologne was funded

by the Deutsche Forschungsgemeinschaft (DFG, German Research Foundation) - Project number 277146847 - CRC 1238 (Subproject A04).

Author contributions

This study was designed by I.K., S.Y., and Y.M.; I.K. performed resistivity measurements and analyses, with the assistance of S.Y. and the guidance of Y.M.; Z.W. and Y.A. grew single crystalline samples and characterized them. The uniaxial strain cell was designed and constructed by I.K.; The manuscript was prepared mainly by I.K. and S.Y., based on discussion among all authors.

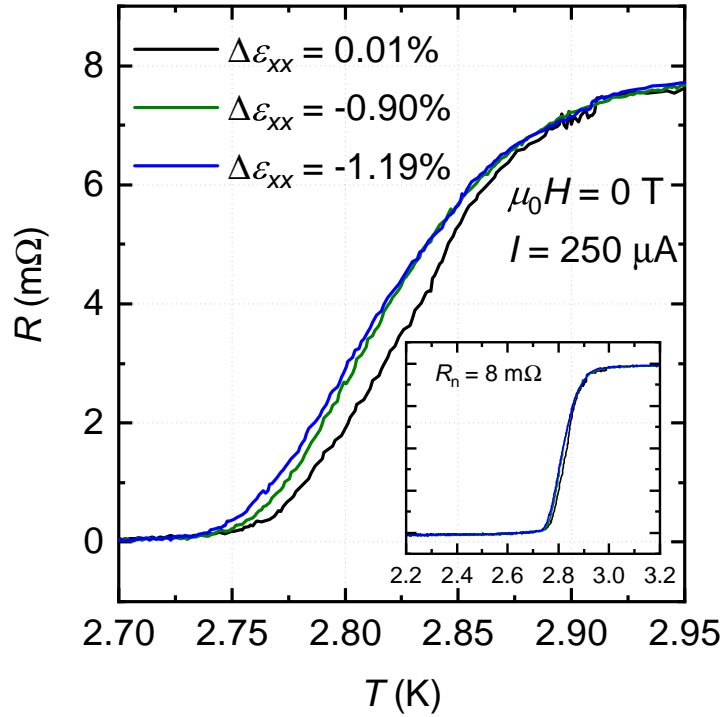
Competing financial interests

All authors declare there is no competing interests regarding this work.

Supplementary Note

S1 Temperature dependence of resistivity at zero field

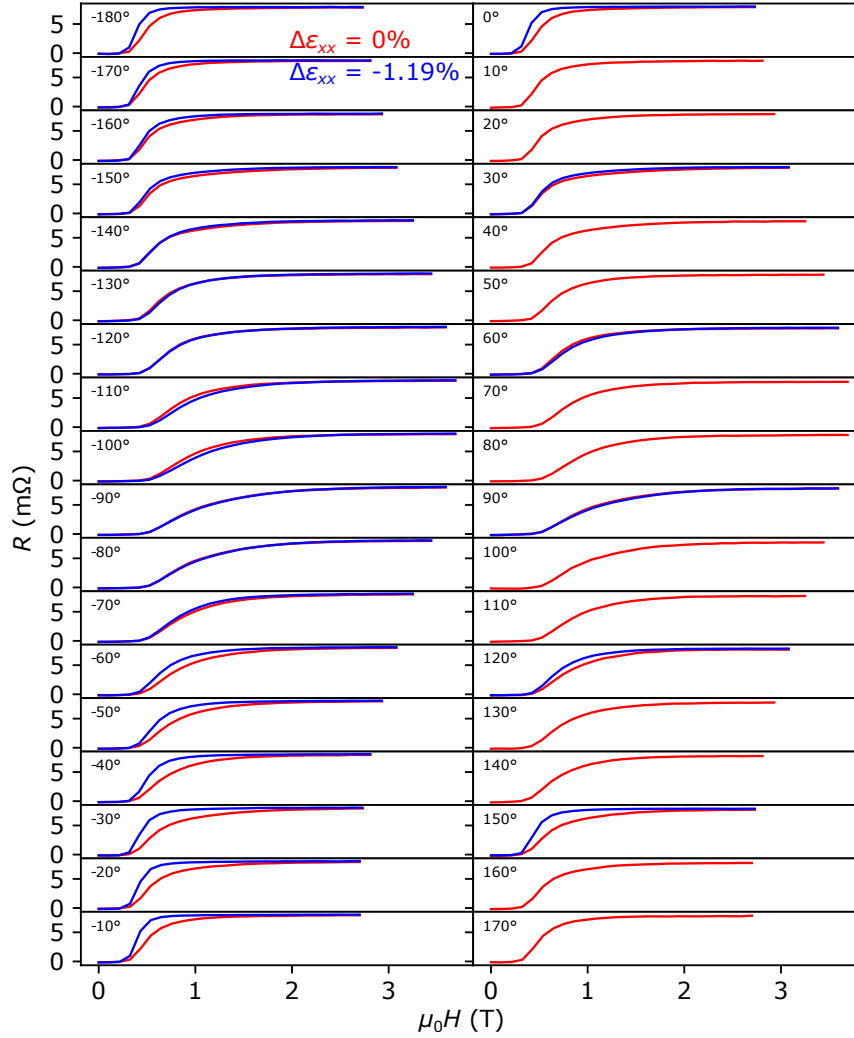
In Fig. S1, we show the temperature dependence of the zero-field resistance of $\text{Sr}_{0.06}\text{Bi}_2\text{Se}_3$ at three different strain values. For these measurements, we used the applied current of $250\text{ }\mu\text{A}$. The superconducting critical temperature (T_c) defined as the mid-point of the transition is 2.83 K for zero relative strain $\Delta\epsilon_{xx}$, i.e. zero applied voltage to the piezo stacks. With increasing $|\Delta\epsilon_{xx}|$, T_c tends to decrease (See Supplementary Fig. S7). With compressive strain of $\Delta\epsilon_{xx} = -1.19\%$, T_c decreases weakly by about 12 mK .



Supplementary Figure S1: Temperature dependence of resistance at zero field and at various applied strain for $\text{Sr}_{0.06}\text{Bi}_2\text{Se}_3$. These data were taken with the applied current I of $250\text{ }\mu\text{A}$. In the inset, larger temperature range is shown to demonstrate the nearly T -independent resistance in the superconducting ($T < 2.7\text{ K}$) and normal state ($T > 2.95\text{ K}$) regions. $R_n = 8\text{ m}\Omega$ is the resistance in the normal-state. The main figure and its inset share the same vertical axis scale.

S2 Raw R vs B data for all in-plane field angles

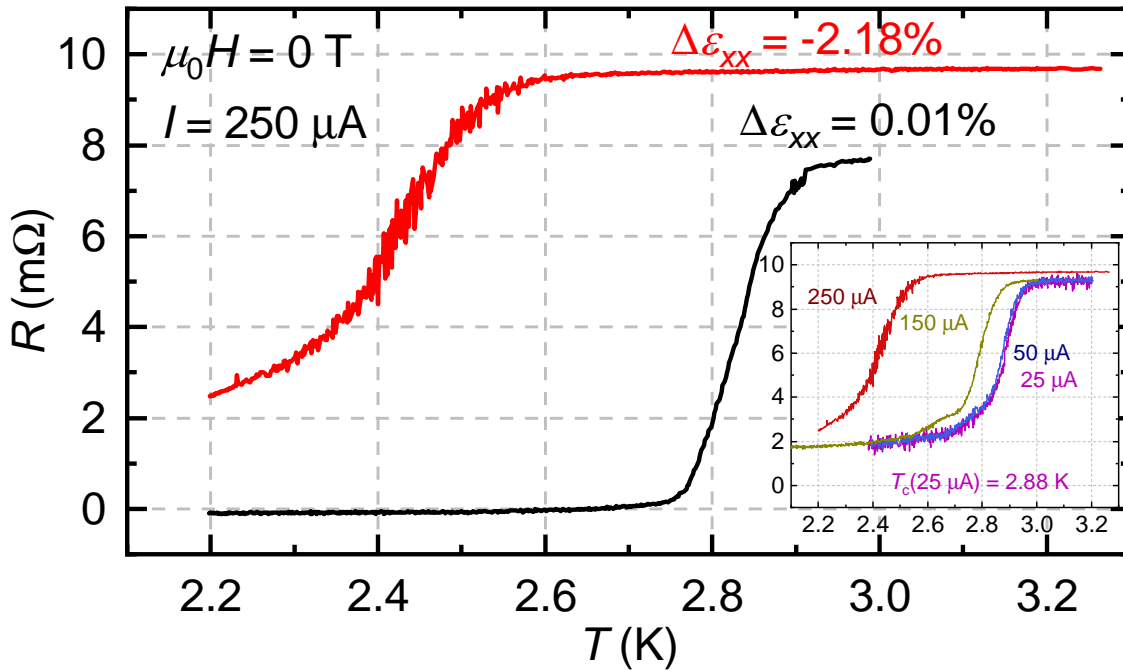
Here, we present a part of the raw magnetoresistance data, which are used to construct the color polar plot (Figs. 2a and b) and to evaluate H_{c2} . In Fig. S2, we show the in-plane magnetoresistance of $\text{Sr}_{0.06}\text{Bi}_2\text{Se}_3$ for field angles in the range of -180° to 170° in steps of 10° . It is clear that with compressive strain of $\Delta\epsilon_{xx} = -1.19\%$, H_{c2} as well as the transition width decreases for $H \parallel x$ ($\phi_{ab} = 0^\circ$ and -180°). Similar strain effect is also observed for the angles corresponding to the large H_{c2} direction of the minor domains (i.e. $\phi_{ab} = \pm 30^\circ$ and $\pm 150^\circ$).



Supplementary Figure S2: Magnetoresistance for various in-plane field angles. The red and blue curves correspond to zero applied strain ($\Delta\epsilon_{xx} = 0$) and compressive strain ($\Delta\epsilon_{xx} = -1.19\%$), respectively.

S3 Irreversible limit of the deformation

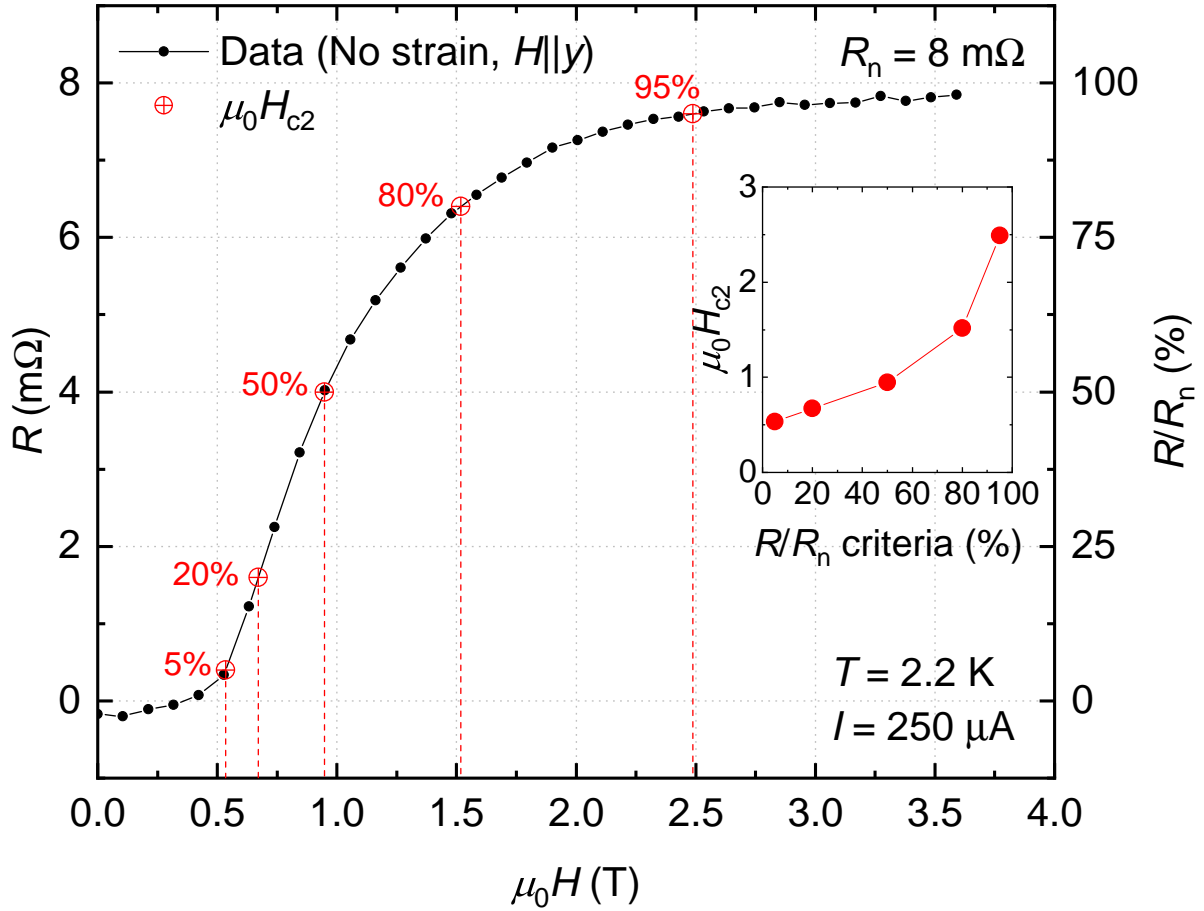
The strain range discussed in the Main Paper (i.e. $-1.5\% < \Delta\epsilon_{xx} < +0.6\%$) is in the elastic deformation regime as evidenced by the reversible change of H_{c2} (Fig. 3). To support this claim, we sought for a border between the elastic and plastic regimes by applying stronger strains. Indeed, as shown in Fig. S3, we found that, after applying a sufficiently large compressive strain, the sample's electrical properties change irreversibly. After applying a large compressive strain of $\Delta\epsilon_{xx} = -2.18\%$, the normal-state resistance increased by about $2\text{ m}\Omega$ and T_c shifts down to about 2.4 K ($\Delta T_c \sim -0.4\text{ K}$), although T_c can be increased again by reducing the applied current from $250\text{ }\mu\text{A}$ down to $50\text{ }\mu\text{A}$. The shift of the normal state resistance persisted after releasing the strain. The likely explanation is that formation of microcracks in the sample increases overall resistance and results in a Josephson-junction-like structure, which has much smaller critical current than bulk.



Supplementary Figure S3: Zero-field resistance versus temperature before and after irreversible change. The black and red curves correspond to zero applied strain and large compressive strain, respectively. (inset) Resistivity curves measured with various currents after the irreversible change. The critical temperature returns close to the original value ($T_c = 2.88\text{ K}$) by decreasing applied current down to $50\text{ }\mu\text{A}$.

S4 H_{c2} criteria

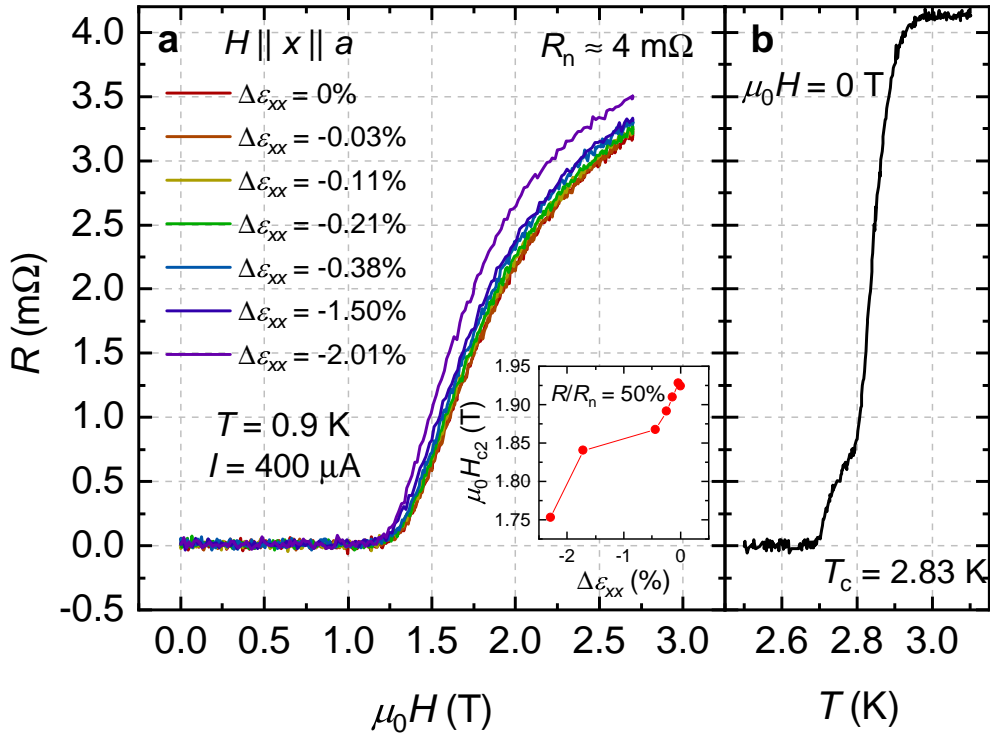
In order to explain H_{c2} evaluated in this work, we show in Fig. S4 an example how H_{c2} is determined from magnetoresistance curves using the criteria in the ratio between the resistance R and its normal-state value R_n . The process is to first decide on a criterion value of R/R_n , e.g. 50%. Then the $R(H)$ curve is linearly interpolated in-between points to determine the precise value of the magnetic field at which R/R_n reaches the criterion value: this value is taken to be H_{c2} of that criterion. In this work, we employ criteria R/R_n ranging from 5% to 95% to carefully examine the strain effect on nematic superconductivity.



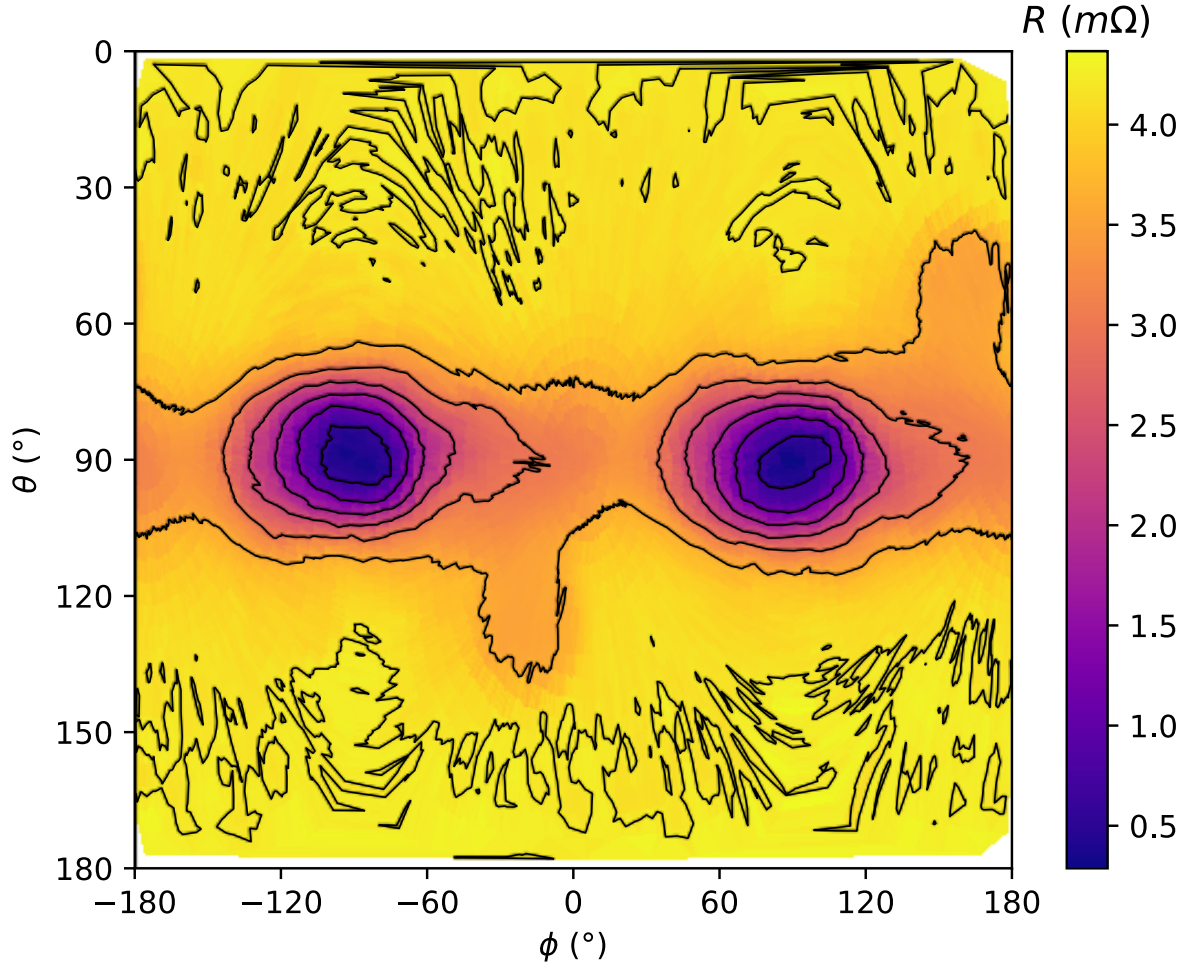
Supplementary Figure S4: Methodology for determining the upper critical field H_{c2} from magnetoresistance data. The data were taken under $\Delta\varepsilon_{xx} = 0\%$ and for $H \parallel y$ ($\phi_{ab} = -90^\circ$). The red percentage labels indicate the R/R_n criteria used, where R_n is the normal-state resistance. The red circle and the corresponding vertical dotted line indicate the resistance value at the criteria and the corresponding field value (to be used as H_{c2}), respectively. (Inset) H_{c2} as a function of the R/R_n criteria.

S5 Reproducibility of the strain control of nematic superconductivity

It is important to show that the strain control of the nematic superconductivity is reproducibly observed in other samples. In Fig. S5, we show the resistance and upper critical field (H_{c2}) of another sample (now referred to as Sample #2) of $\text{Sr}_{0.06}\text{Bi}_2\text{Se}_3$. The strain dependence of $H_{c2} \parallel x$ of Sample #2 is qualitatively similar to that of Sample #1, the sample that is mainly discussed in this Letter: a decreasing trend of $H_{c2} \parallel x$ with compressive strain. The strain effect is less significant in this sample, likely because the sample is already in a nearly single-domain state without the external strain. Indeed, in Fig. S6, the contour plot of magnetoresistance as functions of the polar and azimuthal field angles, we can see that the six-fold behavior due to minor domains is rather weak in Sample #2, compared with the similar plot of Sample #1 (Supplementary Fig. S9b).



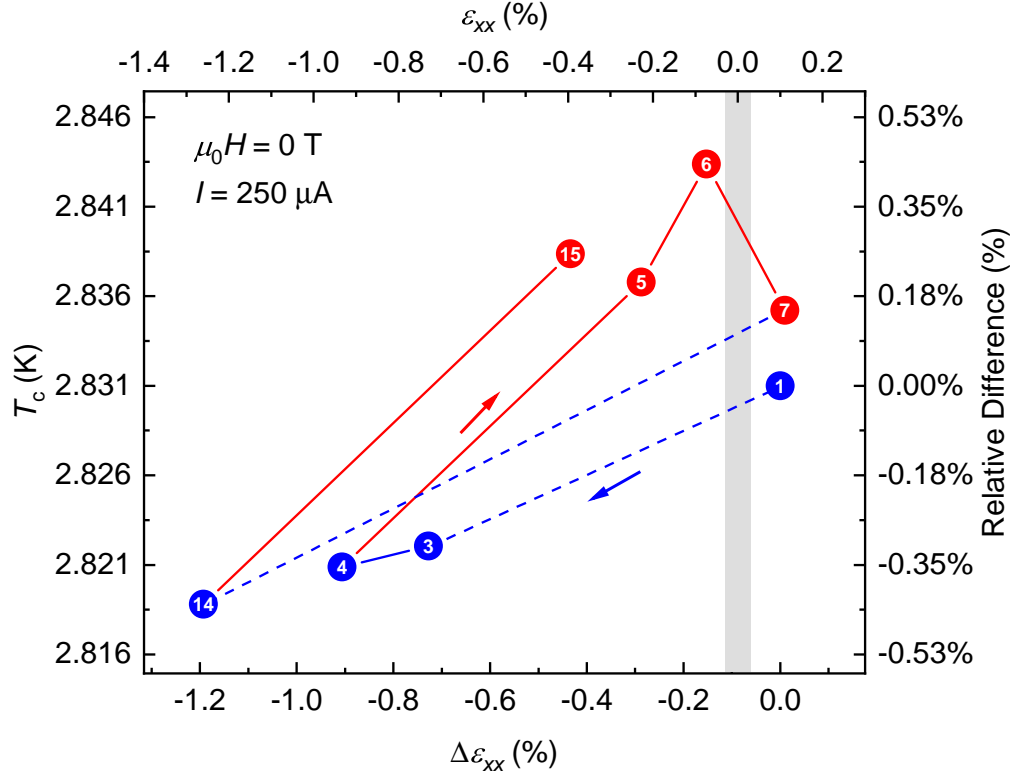
Supplementary Figure S5: Reproducibility of the strain control of nematic superconductivity of Sample #2. **a**, Magnetoresistance measured at 0.9 K and for $H \parallel x$ under various strains. The upper critical field evaluated from these curves (using the criteria $R/R_n = 50\%$) is shown in the inset as a function of $\Delta\epsilon_{xx}$. Note that with increasing compressive strain the upper critical field tends to decrease. **b**, Zero-field temperature dependence of the resistance. For this sample, T_c evaluated at 50% of the transition is 2.83 K, which is very close to that of Sample #1.



Supplementary Figure S6: Polar and azimuthal magnetic field dependence of resistance of Sample #2 at zero strain. The two-fold nematic SC component in the basal plane ($\theta = 90^\circ$) is clearly seen. Notice that the contours around the purple region have oval shape, nearly free from dips at $\phi_{ab} = \pm 30$ and $\pm 150^\circ$. This fact indicates that contributions from minor domains are much weaker in this sample than in Sample #1. The data here were taken at $\mu_0 H = 2.7$ T, $T = 0.9$ K, and $I = 400 \mu\text{A}$.

S6 Strain dependence of T_c

To see the strain dependence of superconducting properties other than the upper critical field, we show in Fig. S7 the dependence of the superconducting critical temperature T_c on the applied strain at zero field. Here, T_c is defined as the midpoint of the transition. We find a decreasing trend of T_c with compressive strain but the overall change is less than 1%. The change in T_c may be due to a change in the density of states, as reported in the hydrostatic-pressure study of $\text{Sr}_{0.06}\text{Bi}_2\text{Se}_3$ ³³.



Supplementary Figure S7: Superconducting critical temperature versus applied strain at zero field.

The numbers in the data points indicate the order of the measurements. The lines also indicate the measurement order. Among them, the dotted lines indicate that the measurement sequence number increases by more than 1, because zero-field resistance measurement was not performed between these measurement sequences. The blue and red data points indicate the cases that the measurement was performed after a decrease and increase in applied strain, respectively. The relative difference in the right vertical axis is defined as the change in T_c from the zero strain T_c (2.831 K).

S7 Rotation of the nematic direction by applied uniaxial strain based on the Ginzburg-Landau theory

The Ginzburg-Landau (GL) free energy on the coupling between the nematic superconductivity and a uniaxial strain under existence of a pre-existing symmetry-breaking field (SBF) is given by²⁸

$$f_{\text{SB}} = (g\vec{\varepsilon} + g_0\vec{\varepsilon}_0) \cdot \vec{S}, \quad (\text{S1})$$

where $\vec{\varepsilon}$ is the applied strain vector, $\vec{\varepsilon}_0$ is the pre-existing SBF vector, \vec{S} is the director of the nematic superconductivity, and g and g_0 are the coupling constants. The strain and SBF vectors are expressed as

$$\vec{\varepsilon} = \begin{pmatrix} \varepsilon_{xx} - \varepsilon_{yy} \\ -2\varepsilon_{xy} \end{pmatrix} = U \begin{pmatrix} \cos(-2\phi) \\ \sin(-2\phi) \end{pmatrix}, \quad (\text{S2})$$

and

$$\vec{\varepsilon}_0 = U_0 \begin{pmatrix} \cos(-2\phi_0) \\ \sin(-2\phi_0) \end{pmatrix}, \quad (\text{S3})$$

where U is the magnitude of applied anisotropic strain, U_0 is the magnitude of the pre-existing SBF, ϕ is the angle of the strain within the basal plane of Bi_2Se_3 , and ϕ_0 is the angle of the pre-existing SBF. The nematic SC order parameter is expressed as

$$\vec{\eta} = \begin{pmatrix} \eta_x \\ \eta_y \end{pmatrix} = \eta \begin{pmatrix} \cos \phi_\eta \\ \sin \phi_\eta \end{pmatrix}. \quad (\text{S4})$$

With this notation, the \vec{S} vector has the form

$$\vec{S} = \begin{pmatrix} |\eta_x|^2 - |\eta_y|^2 \\ -2\eta_x\eta_y \end{pmatrix} = \eta^2 \begin{pmatrix} \cos(-2\phi_\eta) \\ \sin(-2\phi_\eta) \end{pmatrix}. \quad (\text{S5})$$

Substituting (S5), (S2), and (S3) into (S1), then (S1) simplifies to

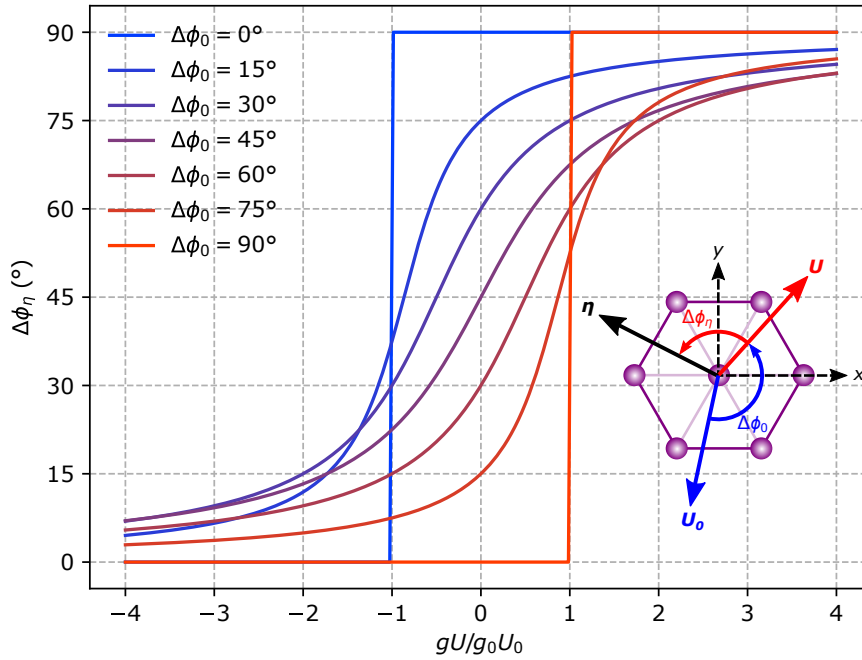
$$f_{\text{SB}} = \eta^2 [gU \cos(2(\phi_\eta - \phi)) + g_0U_0 \cos(2(\phi_\eta - \phi_0))]. \quad (\text{S6})$$

The nematicity direction ϕ_η is chosen such that the free energy is minimized (i.e. $df_{\text{SB}}/d\phi_\eta = 0$ and $d^2f_{\text{SB}}/d\phi_\eta^2 > 0$):

$$\Delta\phi_\eta = -\frac{1}{2} \arctan \left(\frac{\sin(2(\Delta\phi_0))}{gU/g_0U_0 + \cos(2(\Delta\phi_0))} \right) + \frac{\pi}{2}k, \quad (\text{S7})$$

where $\Delta\phi_\eta \equiv \phi_\eta - \phi$ is the nematicity direction with respect to the applied strain direction, $\Delta\phi_0 \equiv \phi - \phi_0$ is the angle between the strain and the pre-existing SBF, and k is an integer chosen such that $d^2 f_{\text{SB}}/d\phi_\eta^2 > 0$ is satisfied.

The result of the above equation (S7) is shown in Fig. S8. It is evident that, when the angle between the applied strain and the pre-existing SBF is orthogonal ($\Delta\phi_0 = 90^\circ$), the nematic direction changes discontinuously when the applied strain term is equal to the pre-existing SBF term (i.e. $gU = g_0U_0$). When the pre-existing SBF is parallel ($\Delta\phi_0 = 0^\circ$), the nematic direction changes suddenly when the applied strain term is equal and opposite to the pre-existing SBF term (i.e. $gU = -g_0U_0$). At intermediate angles, the direction of the nematicity changes continuously but rapidly until the ratio of the applied and pre-existing SBF, gU/g_0U_0 , reaches about 1, after which it changes more gradually. This rotation is very likely the driving force of the nematic domain change under uniaxial compression observed in this work.



Supplementary Figure S8: Rotation of the nematic direction by applied uniaxial strain. The uniaxial strain with the magnitude U is applied at an angle $\Delta\phi_0$ from the pre-existing symmetry breaking field (strength U_0). $\Delta\phi_\eta$ is the angle relative to the axis of the applied strain. The inset shows the definitions of the axes and the symmetry breaking fields (U , U_0) and nematic director (η) with respect to the crystal structure in the ab plane.

S8 Transformation between the laboratory and sample frames

In this section, we describe the procedure to determine the transformation relation between the sample and laboratory frames, to align magnetic fields accurately with respect to the crystalline axes.

In this work, the magnetic field was applied using a vector-magnet system, which consists of two orthogonal superconducting magnets: one pointing in the vertical direction and the other in the horizontal direction in the laboratory frame³⁶. The polar and azimuthal angles of the magnetic field are indicated by θ_{Lab} and ϕ_{Lab} , respectively. To know the transformation between the laboratory frame angles (θ_{Lab} and ϕ_{Lab}) and the sample frame angles (θ and ϕ), we made use of the anisotropy in H_{c2} . We first measured the angular magnetoresistance in the superconducting transition region, covering the full 4π solid angle of the magnetic field, as shown in Fig. S9a in the laboratory frame. Because H_{c2} of $\text{Sr}_x\text{Bi}_2\text{Se}_3$ is smallest along the c axis⁸, the field direction with the largest resistance is the c direction and the plane with relatively small resistance should be the ab plane. If this data is correctly transformed into the sample frame by using a 3×3 rotation matrix R , the former should be located at $\theta = 0$ or 180° , and the latter should lie at $\theta = 90^\circ$. Thus, our goal is to find such a matrix R .

In general, a vector in the laboratory frame v_{Lab} transforms to a vector in the sample frame v via:

$$v = R \cdot v_{\text{Lab}}. \quad (\text{S8})$$

The vectors v and v_{Lab} are in Cartesian coordinates. The rotation matrix R can be decomposed into three elemental rotation matrices with the Euler angles α, β , and γ :

$$R = Z(\gamma)X(\beta)Z(\alpha), \quad (\text{S9})$$

which corresponds to the combination of a rotation by α about z axis, then a rotation by β about the rotated x axis, and then a rotation by γ about the rotated z axis. Note that the elemental rotation matrices are given as follows:

$$X(\omega) = \begin{pmatrix} 1 & 0 & 0 \\ 0 & \cos \omega & -\sin \omega \\ 0 & \sin \omega & \cos \omega \end{pmatrix} \quad (\text{S10})$$

$$Z(\omega) = \begin{pmatrix} \cos \omega & -\sin \omega & 0 \\ \sin \omega & \cos \omega & 0 \\ 0 & 0 & 1 \end{pmatrix}, \quad (\text{S11})$$

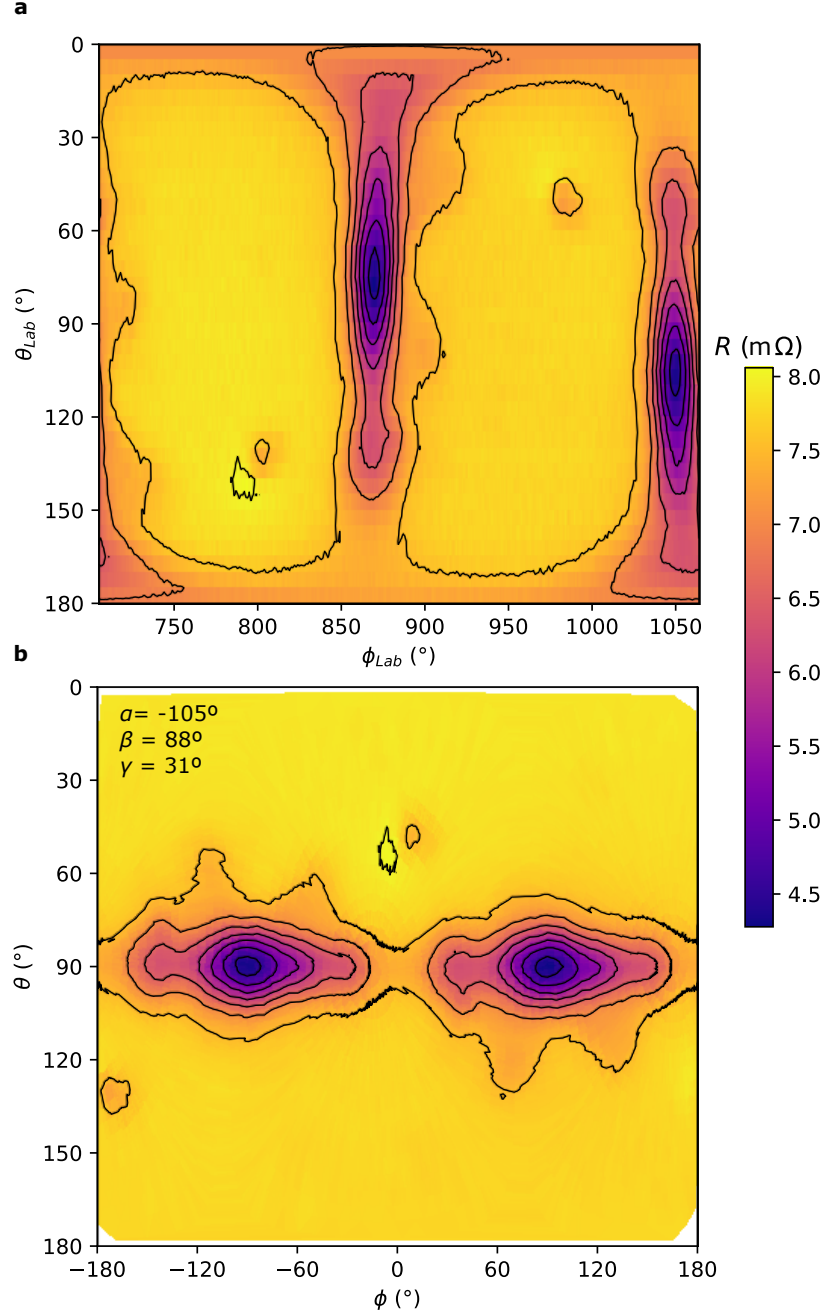
where ω is one of the Euler angles. Lastly, the sample frame vector v is converted from Cartesian to spherical coordinates defined by the two variables θ and ϕ . The basal plane ϕ_{ab} is given as ϕ on the plane of $\theta = 90^\circ$.

When determining the Euler angles from the experiment, we first find the plane of low resistance (i.e. the ab plane) comes on the plane $\theta = 90^\circ$ when we used the Euler angles $\alpha = -105^\circ$ and $\beta = 88^\circ$. To determine γ , we need to use the fact that the sample's x axis (one of the a axes) is roughly oriented along $\theta_{Lab} = 0^\circ$, as described in Methods. This x axis should be transformed to $\phi = 0^\circ$ in the $\theta = 90^\circ$ plane after the γ rotation. This determines the last Euler angle γ to be 31° . With this combination of the Euler angles, the angular magnetoresistance is now transformed as shown in Fig. S9b, matching with the expectation explained above.

Finally, the magnetic field coordinate matrices expressed in the sample frame H_{Sample} and that in the laboratory frame H_{Lab} can be converted back and forth via the relation

$$H_{\text{Sample}} = R \cdot H_{\text{Lab}}. \quad (\text{S12})$$

As mentioned in Methods, the magnetic field presented in the Main Text are all expressed in the Sample frame determined in this way.



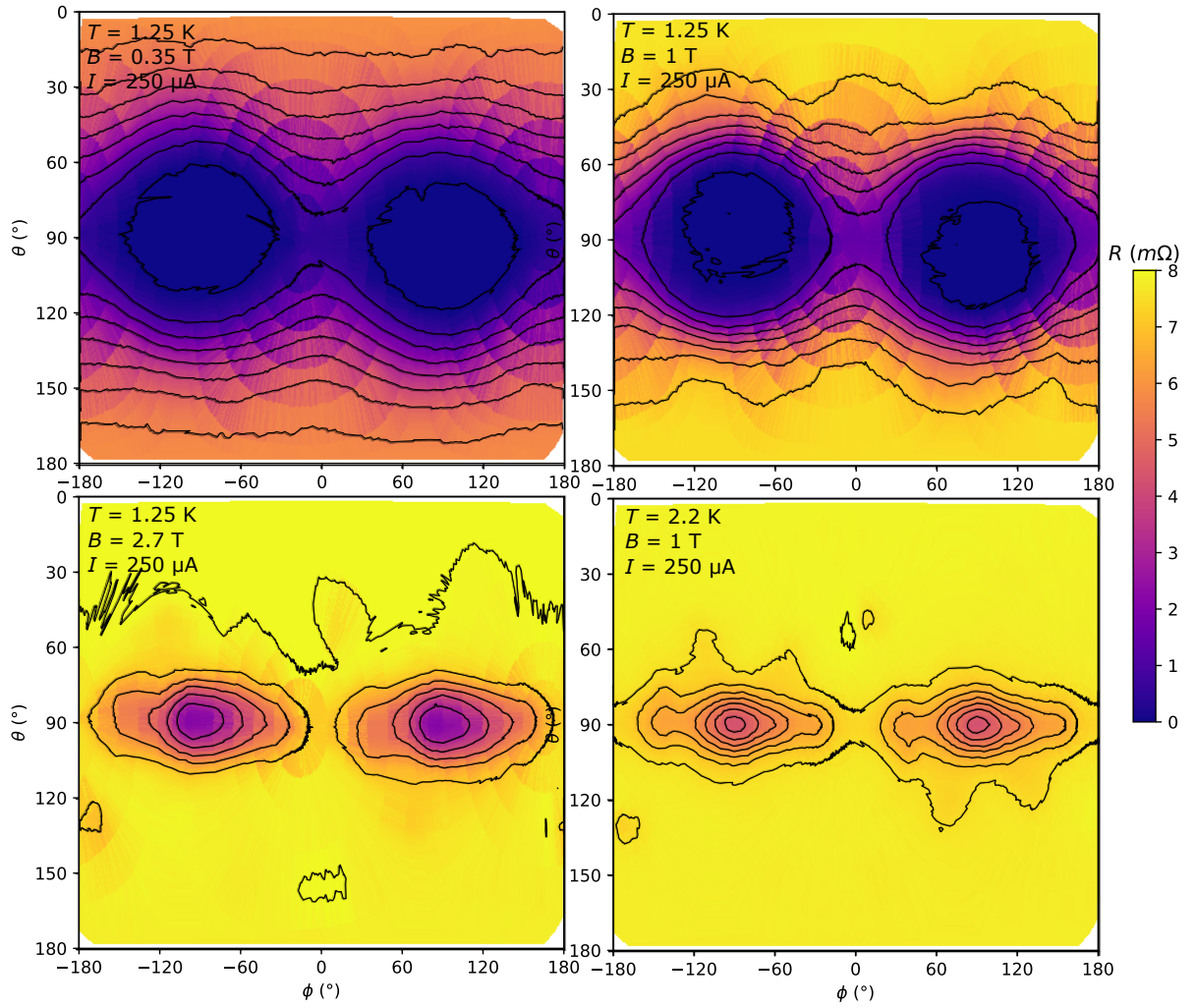
Supplementary Figure S9: Euler transform from laboratory to sample frame. **a**, Contour plot of the angular magnetoresistance plotted as functions of the azimuthal and polar field angles in the laboratory frame. The data were obtained at 2.2 K and 1 T. **b**, Same data plotted as functions of field angles in the sample frame, after rotating the data by using the Euler angles ($\alpha = -105^\circ$, $\beta = 88^\circ$, $\gamma = 31^\circ$).

S9 Angular magnetoresistance at zero applied strain

In this section, we show angular magnetoresistance covering the whole 4π solid angles of the field directions at zero applied strain, in order to demonstrate that the observed behavior is not due to the field misalignment.

In Fig. S10, we show the colour plots of the magnetoresistance as functions of the polar and azimuthal field angles, measured at different magnetic field strength and temperature at zero applied strain (i.e. $\Delta\epsilon_{xx} = 0\%$). Evidently, for all cases the strong two-fold behavior along the ϕ direction due to the nematic superconductivity is seen. For low temperature and/or low field, most of the angles are largely in the superconducting state (corresponding to the dark-blue region), whereas for high temperature or high field only the regions with largest upper critical field remain in the superconducting state. From these data, we confirm that our alignment of the magnetic field to the crystal axis is quite accurate and field-misalignment effect is negligible.

In addition to the strong two-fold behavior, the data near the onset (the two bottom panels of Fig. S10) exhibit small anomalies at around $\phi = \pm 30^\circ$ and $\pm 150^\circ$. See that some contours have dips at these angles. These anomalies are due to the existence of nematic subdomains as discussed in the Main Text.



Supplementary Figure S10: Polar and azimuthal angle dependences of the magnetoresistance at zero strain for various magnetic-field and temperature conditions. The light yellow and dark blue regions correspond to normal state and superconducting state, respectively. Measurement conditions are indicated in the top-left corner of each panel.

S10 Model simulation

In order to simulate the magnetoresistance and the upper-critical-field behavior under single and multiple nematic SC domains, we performed a model simulation. In this section, details of the simulation will be discussed.

Magnetoresistance of each domain

Firstly, we have to define the magnetoresistance behavior of each domain. We assumed that the magnetoresistance of a single nematic SC domain obeys the following empirical equation:

$$\frac{R(H, \phi_{ab})}{R_{n0}} = \left[1 + \left(\frac{H}{H_{c2}(\phi_{ab})} \right)^{-h(H_{c2}(\phi_{ab}))} (2^{1/s} - 1) \right]^{-s}, \quad (\text{S13})$$

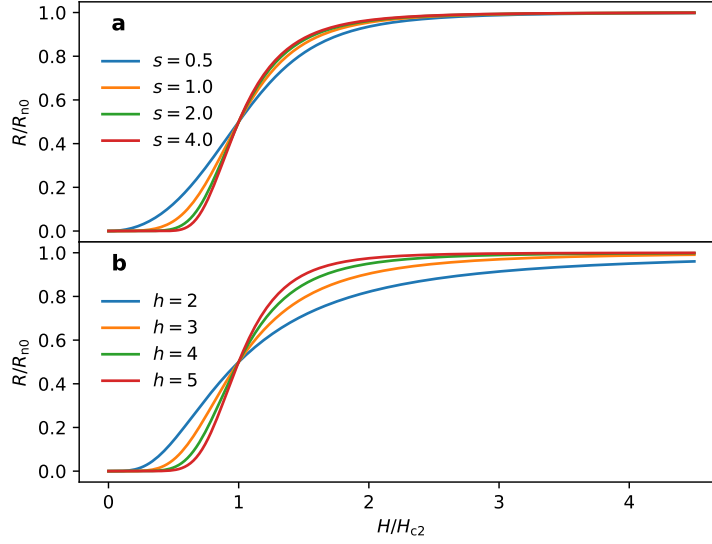
where R_{n0} is the normal state resistance of the domain, ϕ_{ab} is the in-plane field angle, H_{c2} is the upper critical field (midpoint), s is an exponent determining the shape of the $R(H)$ curve around H_{c2} , and $h(H_{c2})$ is another exponent introduced to depict the H_{c2} -dependent transition width. Notice that the coefficient $2^{1/s} - 1$ is a correction factor to make the right-hand side of eq. (S13) to 1/2 at $H = H_{c2}(\phi_{ab})$. The functional form of the right-hand side of eq. (S13) is shown in Fig. S11.

For the actual simulation, we used the exponent $s = 2.03535$ and we employed an empirical relation $h(H_{c2}) = -2.696 \times H_{c2}(\phi_{ab}) / H_{c2,\max} + 5.74248$ to reproduce the observed resistance behavior of the actual sample, in particular the H_{c2} -dependent broadening of the transition. Here, $H_{c2,\max}$ is the maximum H_{c2} within the ab plane. The angular dependence of H_{c2} is approximated by the anisotropic mass model:

$$H_{c2}(\phi_{ab}) = \frac{H_{c2,\max}}{\sqrt{\cos^2(\phi_{ab} - \phi_0) + \Gamma^2 \sin^2(\phi_{ab} - \phi_0)}}, \quad (\text{S14})$$

where $\Gamma \equiv H_{c2,\max} / H_{c2,\min}$ is the anisotropy, and $H_{c2,\min}$ is the minimum H_{c2} given by $\phi_{ab} = \phi_0 \pm \pi/2$. The value of ϕ_0 defines the nematic superconducting domains: For the Y_n domain ($n = 0, 1, 2$), ϕ_0 is given by $\pi/2 + n\pi/3$. We found that $\Gamma = 3$ best reproduces the experimental data. Thus, this Γ value is used hereafter. Another important parameter, $H_{c2,\max}$ is set to 1 T unless explicitly mentioned, to reproduce the $R(H)$ curve at 2.2 K.

With these formulations and parameters, eq. (S13) exhibits functional forms shown in Fig. S12 in the case of $\phi_0 = \pi/2$ (Y_0 domain). Comparing these curves with the raw data shown in Fig. 1c, we can see that eq. (S13) well reproduces the observed magnetoresistance of the strained



Supplementary Figure S11: Plot of Eq. (S13), representing resistance versus applied magnetic field for a single domain, for varying parameters. a, For varying s where $h = 4.39$. **b,** For varying h where $s = 2.04$.

sample (corresponding to a single Y_0 domain state). Thus, the formulation described above should be valid for the simulation.

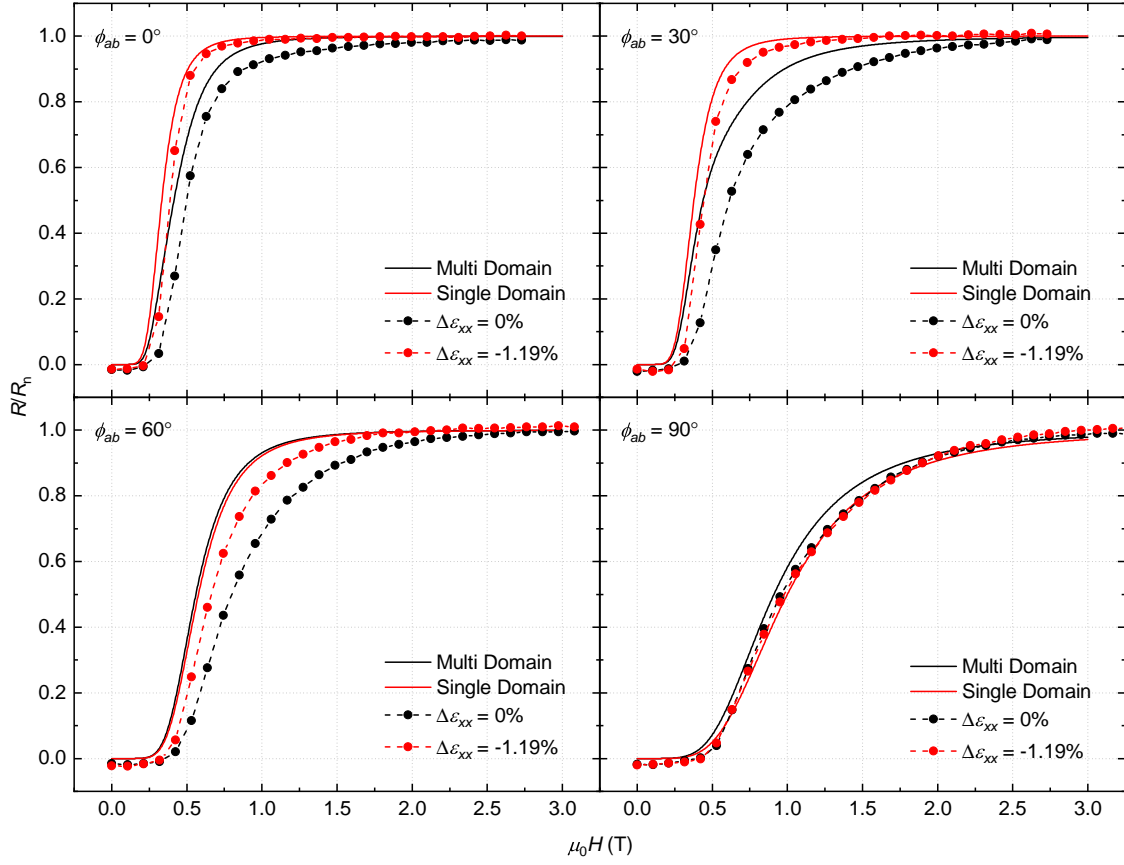
Circuit model of multiple domains

Next, we have to assume a certain circuit to model the distribution of domains. In Fig. S13, we present the electrical circuit model used to produce data in Fig. 4, consisting of a 3D network of twelve resistive elements $R_{1a}, R_{1b}, \dots, R_{2B}$. The end-to-end total resistance of this circuit R_{total} is given by a certain function f :

$$R_{\text{total}}(H, \phi_{ab}) = f(R_{1a}(H, \phi_{ab}), R_{1b}(H, \phi_{ab}), \dots, R_{2B}(H, \phi_{ab})), \quad (\text{S15})$$

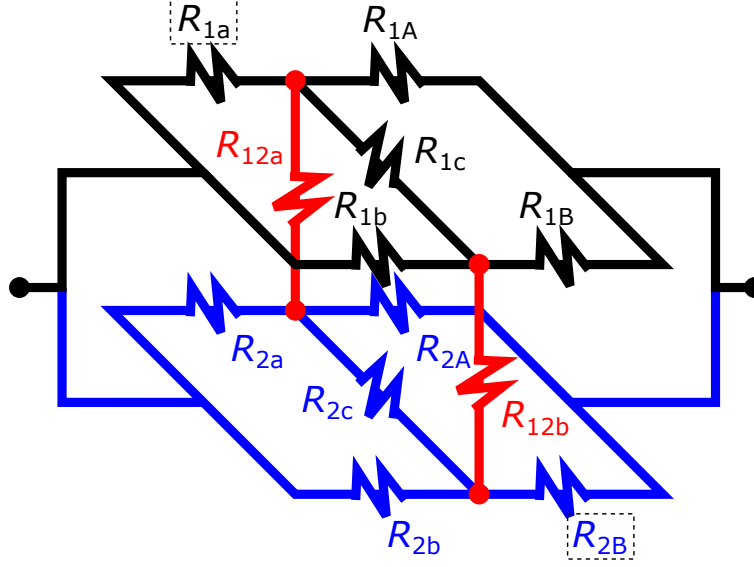
which is determined by standard techniques of circuit analysis. The normal-state resistance $R_{\text{total},n}$ of the net circuit is given by

$$R_{\text{total},n} = R_{\text{total}}(H \rightarrow \infty) \quad (\text{S16})$$



Supplementary Figure S12: Comparison between data and model for R/R_n vs $\mu_0 H$ at different in-plane angles. The angle of the magnetic field is shown by ϕ_{ab} in the top-left corner in each panel. The multi domain model is given by eq. (S15). The single domain model is given by eq. (S13). The nematic anisotropy used is $\Gamma = 3$. The maximum in-plane upper critical field is $\mu_0 H_{c2,\max} = 1$ T.

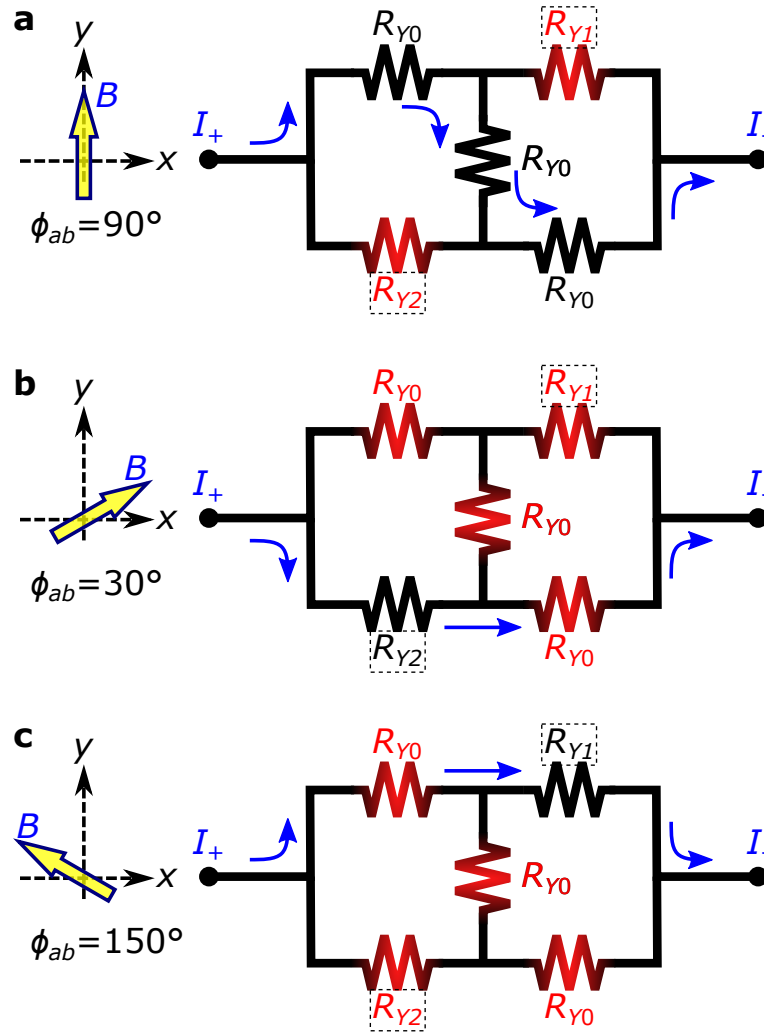
For the multi-domain simulation presented in Fig. 4 of the Main Text, we assumed that R_{1a} and R_{2B} are Y_1 and Y_2 domains and the rest are Y_0 domains. For each domain, the normal-state resistance value R_{n0} is assumed to be the same. Magnetoresistance curves obtained for this multi-domain case are shown in Fig. S12, which captures features of the magnetoresistance of the unstrained sample (i.e. $\Delta\epsilon_{xx} = 0$). For the single-domain simulation, we set all components to the Y_0 domain. We comment that, for the single domain case, $R_{\text{total}}/R_{\text{total},n}$ is identical to R/R_{n0} of eq. (S13).



Supplementary Figure S13: Electrical circuit of a 3D network of resistive elements used for the simulation. The black and blue colored lines represent the top and bottom parts of the circuit, respectively. The red lines are the interconnecting paths between the top and bottom parts of the circuit. The elements marked by the dotted box are set to the minor domains in case of the multi-domain simulation.

Illustrative explanation using a simpler model

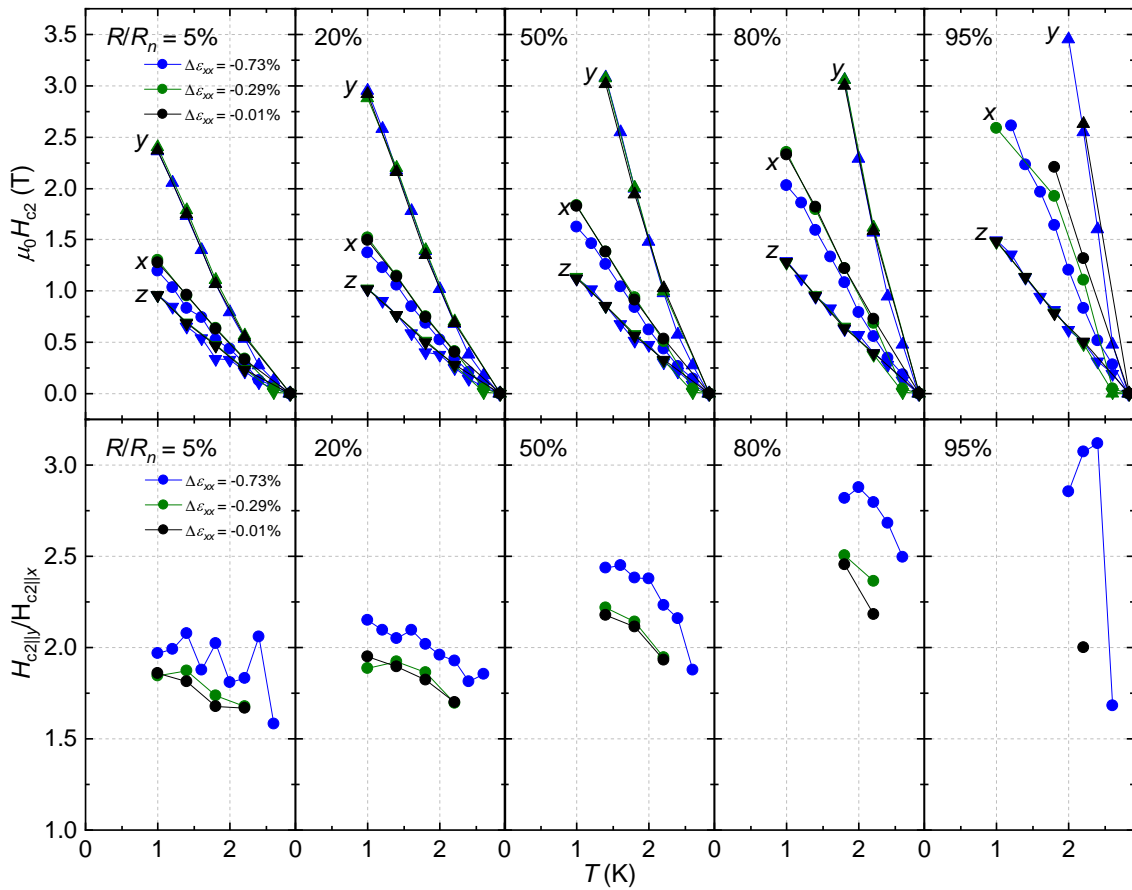
In order to illustrate how the path of the current changes depending on the direction of the applied magnetic field, we show a simplified version of the above circuit in Fig. S14. When the direction of the applied magnetic field is parallel to the axis that has the largest H_{c2} for the dominant domain, Y_0 (Fig. S14a), then the Y_0 domain has lower resistance than the minor domains Y_1 and Y_2 and hence the current passes mostly through the Y_0 domains. If the field angle is aligned with the H_{c2} maximum of either the Y_1 or Y_2 domains (Fig. S14b or c), then the current will certainly pass through those domains. However, due to the configuration of the domains in the network, the current must pass through a Y_0 domain as well to reach the opposite end. This effect is what ensures that the minor domains have a relatively smaller influence on H_{c2} than the dominant domain except for the very vicinity of the onset of superconductivity. Hence we get the characteristic 6-fold in-plane H_{c2} with one of the 2-fold H_{c2} being relatively larger than the other near the onset (95 or 80% criteria H_{c2}) but purely two-fold behavior close to zero resistance state (20 or 5% criteria H_{c2}).



Supplementary Figure S14: Simplified electrical circuit diagrams describing the current path dependence on the direction of the applied field. The black and red color of the resistive element (R) indicate relatively low and high resistance, respectively. The blue arrows indicate the path of the current at each configuration. The yellow arrow indicates the angle (ϕ_{ab}) of the magnetic field (B) relative to the sample's x axis. The three domains are Y_0 , Y_1 , and Y_2 , which are most superconducting at the field angles $\pm 90^\circ$, 150° (-30°), and 30° (-150°). **a.** At $\phi_{ab} = 90^\circ$ R_{Y0} is least resistive and the current passes through the center avoiding R_{Y1} and R_{Y2} . **b.** At $\phi_{ab} = 30^\circ$ R_{Y2} is least resistive so the current initially avoids R_{Y0} but after the first element the current has to pass through the less resistive path that is R_{Y0} (instead of R_{Y0} and R_{Y1}). **c.** same as (b) except for $\phi_{ab} = 150^\circ$ and R_{Y1} is initially preferred. The dotted box indicates the minor domain.

S11 H - T phase diagrams

To describe the temperature evolution of the strain effect, we show in Fig. S15 the temperature dependence of H_{c2} determined with various R/R_n criteria along the three principal axes (x , y , z). We also show the in-plane H_{c2} anisotropy ($H_{c2} \parallel y/H_{c2} \parallel x$) under various strain in the bottom panels. With lowering temperature, H_{c2} exhibits linear increase. The in-plane H_{c2} anisotropy ranges 2-3 depending on the H_{c2} criteria. Such a relatively large anisotropy is consistent with previous studies on Sr-doped Bi_2Se_3 ^{8,22}. With an increase of compressive strain, the H_{c2} anisotropy increases for the whole temperature range investigated. Thus, the uniaxial-strain control of nematic superconductivity is achieved irrespective of the temperature range.



Supplementary Figure S15: Upper critical field H_{c2} (top panels) and in-plane H_{c2} anisotropy (bottom panels) dependence on the temperature for varying applied strain. The colors black, green, and blue correspond to small to larger compressive strains. The numbers in the top corner of each sub-panel indicates the criteria used for determining H_{c2} . Note that at low temperatures there are missing data points due to the magnetoresistance data not having the necessary resistive range for the specified H_{c2} criterion.